



1

2 **Spectroscopic detection of terrestrial lightning from space by JUICE-MAJIS**
3 **during Earth Gravity Assist**

4

5 Emiliano D'Aversa⁽¹⁾, Fabrizio Oliva⁽¹⁾, Giuseppe Piccioni⁽¹⁾, François Poulet⁽²⁾, Ivana
6 Kolmašová⁽³⁾, Alessandra Migliorini⁽¹⁾, Gianrico Filacchione⁽¹⁾, Leigh Fletcher⁽⁴⁾, Alessandro
7 Mura⁽¹⁾, Yves Langevin⁽²⁾, Benoît Seignovert⁽²⁾, Davide Grassi⁽¹⁾, Sébastien Rodriguez⁽²⁾,
8 Federico Tosi⁽¹⁾, Nicolas Ligier⁽²⁾, Giuseppe Sindoni⁽⁵⁾, Marco Giardino⁽⁵⁾, Christina Plainaki⁽⁵⁾

9

10 (1) Istituto Nazionale di Astrofisica, INAF-IAPS, Via del Fosso del Cavaliere 100, 00133, Rome,
11 Italy.

12 (2) Institut d'Astrophysique Spatiale, CNRS/Université Paris-Saclay, 91405 Orsay Cedex,
13 France.

14 (3) Department of Space Physics, Institute of Atmospheric Physics of the Czech Academy of
15 Sciences, Prague, Czechia.

16 (4) School of Physics and Astronomy, University of Leicester, University Road, Leicester, LE1
17 7RH, UK.

18 (5) Italian Space Agency, Via del Politecnico snc, 00133, Rome, Italy.

19

20

21

22

23 Correspondence to: emiliano.daversa@inaf.it

24

25

26

27

28

29

30

31

32

33

34

35

36

37

38

39

40

41

42

43

44

45

46

47



48
49

Abstract

50
51
52
53
54
55
56
57
58

A lightning event was detected by the MAJIS imaging spectrometer onboard the Jupiter Icy Moons Explorer (JUICE) spacecraft during its first Earth gravity assist maneuver. This serendipitous space-based spectroscopic observation represents the first detection of its kind for any planetary atmosphere. The event, composed of four flashes, was registered on 2024, August, 20th in an area offshore of Sumatra island, during local nighttime, near to optically thick clouds probed by MAJIS thermal wavelengths. No coincident detection has been obtained by ground-based lightning sensor networks, yet MAJIS observations provide unambiguous evidence of neutral atomic oxygen and nitrogen emissions, identified through several diagnostic lines. A faint H α signature may also tentatively be associated with lightning flashes.

59
60
61
62
63
64
65

As MAJIS is not optimized for such observations, a number of caveats related to spectral and temporal resolutions have been considered when deriving absolute quantities, such as lightning energy and temperature. Retrieved energies are overall consistent with known emission by lightning of average strength, ranging from (0.7±0.2) to (1.3±0.3) MJ in the 777 nm O I line and from (0.5±0.2) to (1.5±0.4) MJ in the 870 nm N I line. Temperature estimates, more sensitive to observing biases, yield a broad range of values, spanning between 5000 and 20000 K, with standard uncertainties of the order of 2000-3000 K depending on the retrieval method.

66
67
68
69
70

This observation represents a useful benchmark for guiding detection and interpreting possible lightning events on Jupiter, a primary target of the JUICE mission. A preliminary extrapolation of the terrestrial case to the conditions of Jovian atmosphere suggests that H I emissions in the 650 nm and 1870 nm spectral ranges are the most promising for identifying lightning on Jupiter with the MAJIS instrument.

71
72
73
74
75
76
77
78
79
80
81
82
83
84
85
86
87
88
89
90
91
92
93
94
95



96 **1. Introduction**

97

98 In its journey to the Jovian system, the JUICE spacecraft performed a close flyby at
99 Earth (Earth Gravity Assist, EGA) on 2024, Aug, 20, about one day after a similar close
100 encounter with the Moon (Lunar Gravity Assist, LGA). Despite the very low flyby altitude, and
101 the consequent high velocity profile, the maneuver allowed the scientific instruments onboard
102 to acquire several datasets, mainly aimed at testing their performances as well as those of the
103 ground-segment. During EGA, the onboard Moon And Jupiter Imaging Spectrometer (MAJIS)
104 collected 19 scans (data cubes) covering the spectral range 500-5560 nm. An extensive
105 overview of the full sequence from both technical and scientific point of views can be found in
106 Poulet et al. (this issue).

107 In the present work we only focus on the first cube of the EGA sequence, where
108 unexpected emissions were found at visible wavelengths on Earth's nightside. These signals
109 suggest a serendipitous detection of lightning flashes originated in a thunderstorm cloud, whose
110 location and thickness are appreciable in simultaneous thermal imaging.

111 In the following Sect.2 we describe in detail the observations and the adopted methods
112 of analysis. Although the observations are not optimal for physical studies of lightning, we
113 attempt to derive the energies and temperatures involved, by applying specific corrections,
114 assessing a useful framework for investigating possible other similar observations by imaging
115 spectrometers. Main results are mostly presented in Sect.3 and discussed in Sect.4. An
116 overview of lightning spectroscopy on Earth and other planets is presented at the beginning of
117 Sect.4. To our knowledge, MAJIS lightning observations presented in this work constitute the
118 first case of an unambiguous direct spectroscopic observation of lightning from space, on any
119 planet. Conclusions are summarized in Sect.5.

120

121

122 **2. MAJIS observations**

123

124 **2.1. Data description and processing**

125

126 The Moon And Jupiter Imaging Spectrometer (MAJIS) is an imaging spectrometer
127 covering the spectral range 500-5560 nm in two separate channels (VISNIR and IR), with a
128 boundary at a wavelength around 2300 nm. Spectral bands' characteristics are variable
129 depending on instrument setting, with nominal VISNIR FWHMs of the order of 3.5-5.6 nm and
130 sampling of 3.6-3.7 nm/band, and slightly larger values for IR channel (FWHM 6.6-8.5 nm and
131 sampling 6-7 nm/band) (Haffoud et al., 2024). Both channels work with 2-dimensional detectors
132 that, sharing the same field of view, can acquire a variety of spectral scans of a target in a push-
133 broom acquisition scheme. The direction of the field of view during a scan is controlled by either
134 changing the whole spacecraft pointing or by rotating an internal mirror, or both. Descriptions of
135 the instrument, its operations and calibration are detailed in Poulet et al. (2024), Filacchione et
136 al. (2024), Haffoud et al. (2024), Langevin et al. (2024), Rodriguez et al. (2024), Vincendon et
137 al. (2024), and Stefani et al. (2025). Observing geometry reconstruction is based on NAIF-SPICE
138 libraries and tools (Acton, 1996; Acton et al., 2018) and kernels provided by ESASPICE Service
139 (JUICE Operational SPICE Kernel Dataset, 2019).

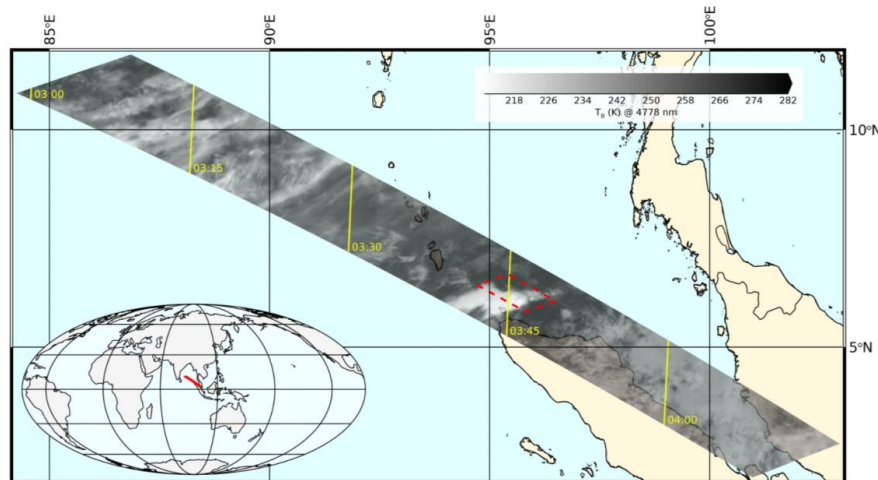
140 While we refer the reader to Poulet et al. (this issue) for a detailed overview of the MAJIS
141 EGA observations, here we only focus on the first data cube of the sequence (UTC start time
142 2024-08-20T21:25:09), where unexpected emissions are seen in the VISNIR channel. No other
143 similar emissions have been found in other data cubes of the same sequence.



144 The cube under investigation covers an area offshore northern Sumatra island, across
145 the Andaman Sea (Figure 1). It is fully registered at nighttime (local time~03:30) hence the
146 presence of clouds can only be appreciated at thermal wavelengths, simultaneously covered by
147 MAJIS IR channel (shown in terms of brightness temperature in the figure). Although the
148 footprint extends over some land areas, no evident variations of thermal emission appear in
149 association with coastlines, suggesting overall cloudy conditions thick enough to prevent land
150 detection.

151 The scan is composed of 128 samples (pixels along slit direction), 865 frames (pixels
152 across slit direction) and 1016 bands (spectral dimension, equally distributed between VISNIR
153 and IR channels), with nominal spatial and spectral binning implemented. It has been obtained
154 by rotating the line of sight by about 4° (2° of rotation of the internal mirror) in 865 steps for a
155 total time of 173 seconds. At every step (i.e. every 200 ms), a 128-pixels spectral frame
156 encompassing 1016 wavelengths has been acquired, with an integration time of 22 ms. The
157 mirror movement caused the ground footprint to move at about 9.4 km/s, spanning almost 10°
158 in latitude (from 11.7°N to 2.0°N). At the same time, the spacecraft was moving rapidly eastward,
159 with a ground projected velocity component of about 6.6 km/s. Since no spacecraft active
160 pointing could be implemented, the resulting MAJIS boresight motion at the ground was at about
161 ~11.5 km/s in the southeast direction, explaining the slant footprint projection shown in Figure
162 1.

163 The area where lightning is detected is near the middle of the MAJIS scan (red box in
164 Figure 1), acquired when the spacecraft was flying at about 11500 km above the surface. In this
165 condition, the MAJIS instantaneous field of view (150 μ rad) is projected to a spatial resolution
166 of about 1.7 km/pixel. However, the motion smearing accumulated during the 22 ms integration
167 yields a slight enlargement of the pixel area by an amount $f \sim 10\%$ (and an average linear
168 resolution degrading to ~ 2 km/pixel).

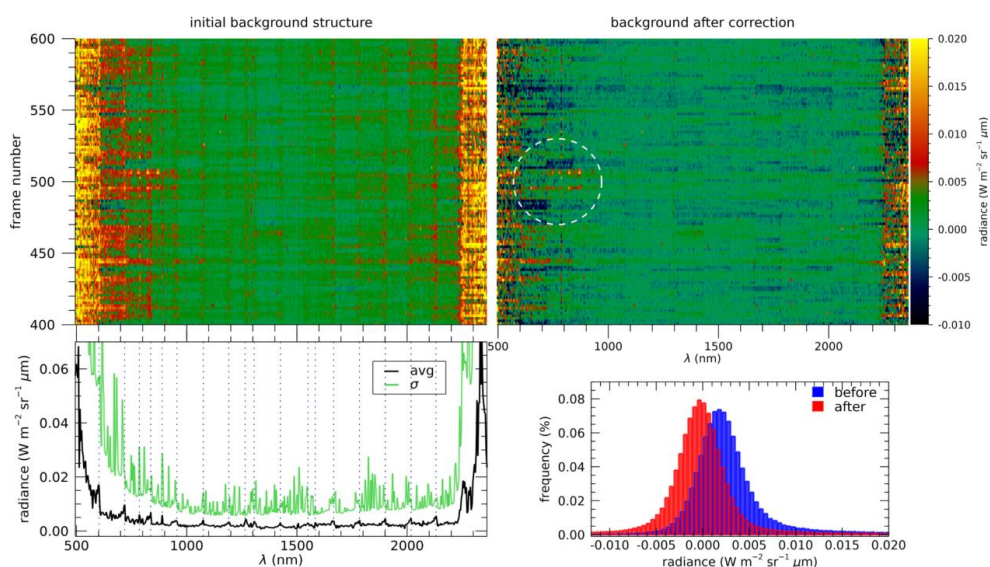


169
170 **Figure 1- Projection of the first MAJIS scan of the EGA sequence, where visible lightning**
171 **emissions are detected. The covered area extends over the Andaman Sea and partially over**
172 **Sumatra island, and Nicobar Archipelago. The gray-scale map represents the brightness**
173 **temperature as registered by MAJIS at 4611 nm wavelength. The red box indicates the area**
174 **of potential lightning detection, detailed in Figure 2.**

175



176 As the data were acquired at nighttime, the signal registered at VISNIR wavelengths
177 outside the lightning area is instrumental noise. The search for potential signatures of known
178 diffuse sources of emission from the Earth atmosphere, like airglows (e.g. the auroral-triggered
179 O I green line at 557.7 nm, Levenko et al., 2019) yields no significant results. This fact simplifies
180 the study of the background fluctuations statistics which is very helpful for deriving absolute
181 intensities and suitable detection thresholds (Noise Equivalent Spectral Radiance, NESR) for
182 lightning emissions. As we can see in Figure 2, the background noise is enhanced at both
183 spectral edges of the VISNIR channel. The subtraction from the data cube of the average
184 spectral background is effective in reducing this issue, narrowing the overall background
185 distribution and allowing lightning signals to emerge more clearly as a statistical anomaly (Figure
186 2). This analysis yields an average detection limit (NESR) for this observation, after background
187 correction, of $2 \cdot 10^{-3}$ $\text{W m}^{-2} \text{sr}^{-1} \mu\text{m}$. It is worth stressing that a significant residual background
188 pattern is still present after correction at the edges of the VISNIR channel, even if limited to the
189 ranges below 700 nm and above 2200 nm.
190



191
192 **Figure 2 - Data preprocessing for background correction.** The VISNIR background for a cube
193 subset encompassing lightning signatures (frames 400-600 and averaged over the samples
194 60-70) are shown in the upper panels, before (upper left) and after (upper right) background
195 correction. Lightning emissions are located near frame 500, highlighted by the dashed ellipse
196 in the upper right panel. The lower left panel shows the spectrum of the average background
197 (black curve) with its standard deviation (green curve). At lower right the comparison of the
198 whole cube background distribution before/after the correction is shown.
199
200
201
202
203
204
205



206
207

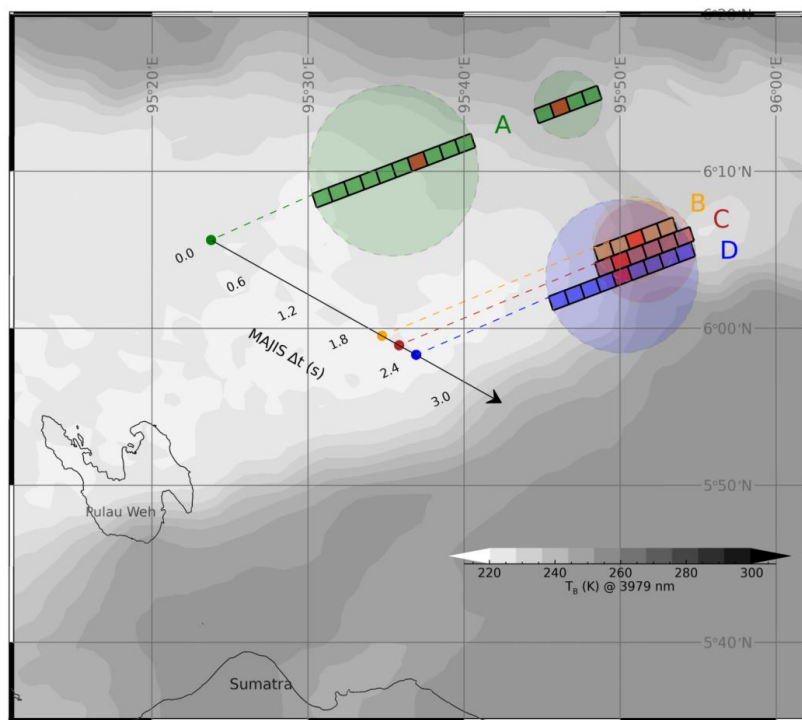
208 2.2. Lightning location and spatial considerations

209

210 The exact locations of lightning signatures are identified by using the radiance thresholds
211 derived from background analysis (see previous Sect.2.1). Figure 3 shows the footprints of
212 those pixels where a signal exceeding 3-times the NESR has been found in more than one
213 spectral band. They are shown projected on the Earth surface against the same thermal image
214 displayed in Figure 1. The pushbroom acquisition scheme implies that, while the instrument
215 boresight moves (in the arrow direction in Figure 3), all pixels along the same spectral frame (A,
216 B, C, D labels in Figure 3) are simultaneously acquired. Therefore, these aligned pixels can
217 actually represent a portion of a larger flash area, whose extension could be guessed from the
218 total length of the illuminated portion of the slit. Assuming a circular shape, the corresponding
219 flash areas extrapolated from the involved MAJIS frames are shown color-shaded in Figure 3.
220 Basic properties of these flashes are given in Table 1. The significant overlapping in the case
221 of B, C and D frames in Figure 3 opens the possibility that MAJIS observed a unique lightning
222 flash sequence there.

223

224 It is worth stressing that this kind of observation cannot resolve the light directly emitted
225 by the lightning channel, which is a few centimeters thick, but is rather sensitive to the light
226 scattered by the surrounding clouds, known to spread for several kilometers from the source.
227 Global statistics report average sizes of scattered lightning flash of about 25 km (e.g. Rudlosky
et al., 2019, give mean areas of 454 km² over land and 570 km² over ocean), close to the lengths
measured in MAJIS flash observations (Table 1), which can therefore be considered as spatially
resolved.



228



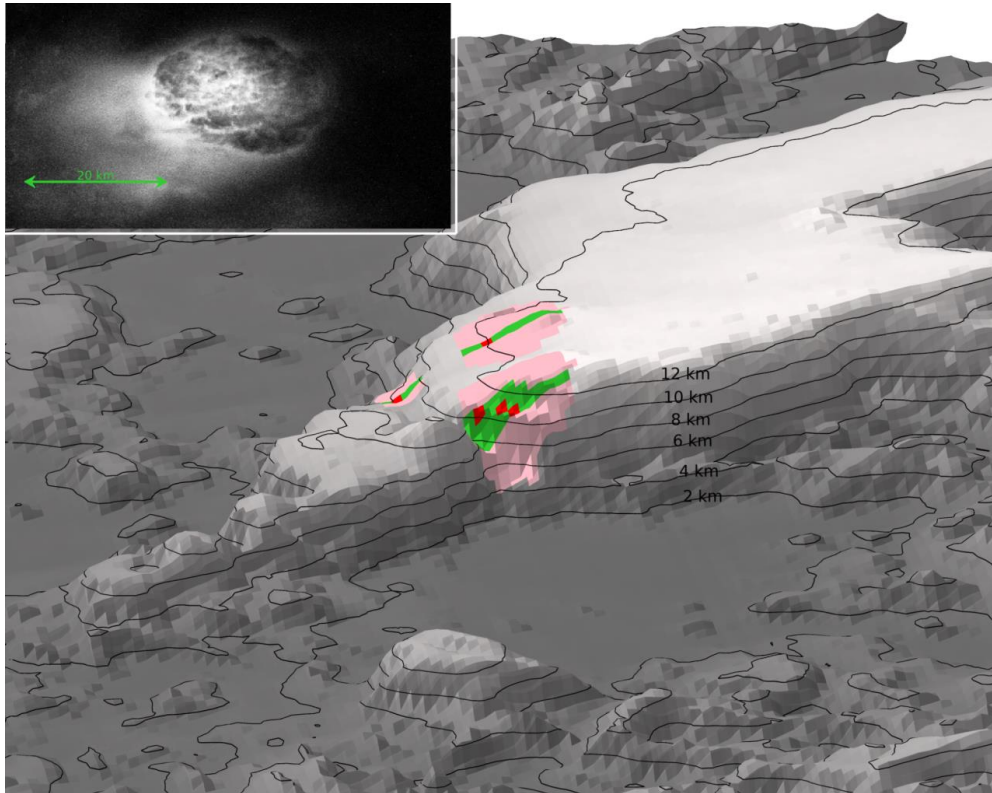
229 **Figure 3**- The footprints of MAJIS lightning pixels are indicated by the colored squares, shown
230 against a brightness temperature map (same of Figure 1). Shaded circles represent the
231 possible lightning flash areas associated with each MAJIS frame (A,B,C,D labels
232 corresponding to frame numbers 494, 504, 505, 506). The red-filled pixels indicate the location
233 of maximum emission at 777 nm for each frame. The arrow highlights the direction of motion
234 of MAJIS boresight and the time delay between detections.
235

236 **Table 1** - Properties of the frame-averaged MAJIS lightning spectra.

flash	MAJIS frame	UTC start	Lon (°)	Lat (°)	flash length (km)
A	494	2024-08-20T21:26:48.47	95.64	6.19	28.2
B	504	2024-08-20T21:26:50.47	95.85	6.09	10.0
C	505	2024-08-20T21:26:50.67	95.86	6.08	12.0
D	506	2024-08-20T21:26:50.87	95.84	6.06	18.1

237
238 The coverage of thermal emission by simultaneous MAJIS IR measurements enables
239 understanding the context where lightning is observed. As highlighted in the papers by Poulet
240 et al. (this issue) and Oliva et al. (this issue), thermal wavelengths can be used to evaluate
241 optical thickness and top altitude of cloud systems. In our case, lightning appears located close
242 to a region having the lowest thermal emission in the whole data cube (i.e. the brightest feature
243 in Figure 1 and Figure 3), revealing the presence of a very thick cloud. Although ice diagnostic
244 signatures are mostly at solar-reflected wavelengths and hence not accessible in this case, the
245 levels of brightness temperatures measured over this cloud is very similar to those found over
246 ice-rich thick cloud systems in other daylight EGA cubes (Oliva et al., this issue), supporting its
247 interpretation as a thunderstorm cloud. By using a representative nighttime vertical thermal
248 profile (taken on 20 Aug 2024 in the nearest station at Banda Aceh¹), the brightness temperature
249 measured by MAJIS (at a wavelength of 4610 nm, poorly absorbed by water vapour), can be
250 converted into an estimate of the cloud top altitude. The result of this analysis is shown in Figure
251 4. This indicates that most of the visible emission is concentrated just along the eastern edge
252 of the thick cloud, whose top lies about 12 km above the surface. The detection near a cloud
253 edge is easily explained by the differential absorption of scattered light inside the cloud, since
254 the reduced optical thickness makes it easier for the lightning's light to escape into space
255 through the cloud boundaries. As a possible analogue, we can refer to lightning images like that
256 in the inset of Figure 4, captured from the orbiting International Space Station, at a spatial scale
257 similar to MAJIS' one.
258

¹ Data downloaded from Wyoming Weather Web, Upperair Air Data, station WITT 96011, University of Wyoming, <https://weather.uwyo.edu/upperair/>.



259
260 **Figure 4:** MAJIS lightning emissions in the context of the clouds seen by MAJIS-IR. Grayscale
261 surface show the cloud top altitude retrieved from thermal emission at $4.61 \mu\text{m}$, labeled using
262 black contour lines. Green regions indicate the MAJIS pixels with lightning signatures
263 (maximum intensity in red areas), while pink shades are the corresponding circular areas
264 (same as in Figure 3). In the inset, a lightning flash imaged in 2021 from the International
265 Space Station, is used as an analogue of the MAJIS observation (Earth Science and Remote
266 Sensing Unit, NASA Johnson Space Center, Photo ID ISS066-E-24707). The horizontal
267 spatial scale (as indicated by the green arrow) is nearly the same in the two images.
268

269 2.3. Lightning spectral identification 270

271 By averaging the spectra of different pixels within the same frame we obtain the 4
272 average spectra shown in Figure 5, corresponding to the parameters listed in Table 1. It is worth
273 stressing that, although small, the motion smearing has been taken into account when summing
274 adjacent spectra. In this case, a correction factor of $1/(1 + 2f) \sim 0.83$ is applied to the radiance
275 averaged along the slit, in order to avoid double-counting the signal coming from the overlapped
276 regions.

277 In Figure 5a the spectra are shown in the full MAJIS wavelength range, with the
278 boundary between the VISNIR and IR channels indicated around 2300 nm. Terrestrial thermal
279 emission dominates the signal longward ~ 3300 nm, spectrally shaped by the vertical profiles of
280 temperature and cloud/aerosols and water opacities, by the broad 4300 nm CO_2 band and by a
281 number of narrower water absorption bands in the 5000 nm range. The 500-1200 nm range,

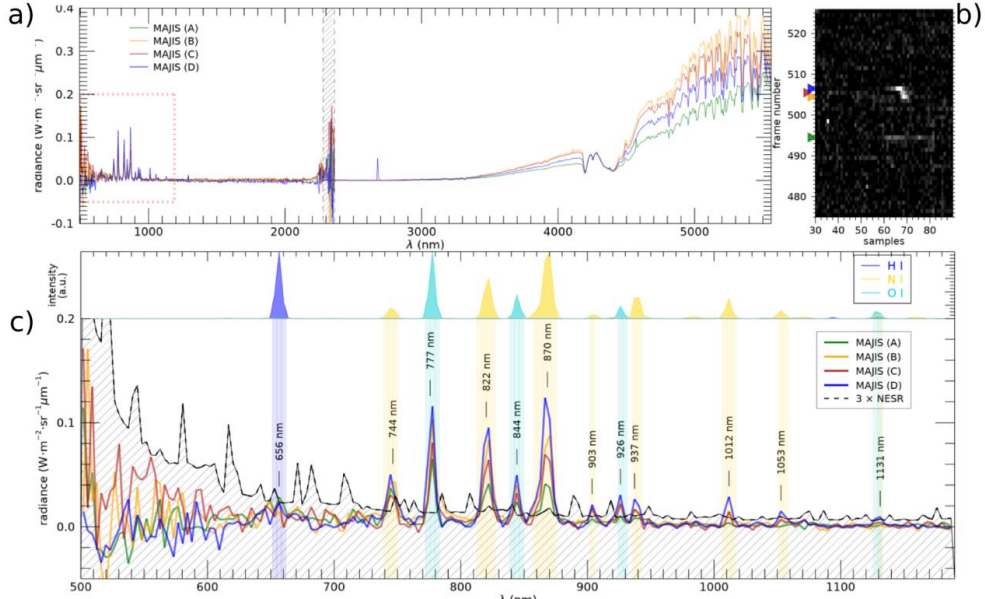


282 blown up in Figure 5c, is characterized by a sequence of rather narrow lines, whose intensity is
283 quite variable from pixel to pixel. The main spectral feature in all spectra is represented by a
284 group of three lines (at 777 nm, 822 nm, and 870 nm), diagnostic of the presence of atomic
285 oxygen and nitrogen typical of terrestrial lightning (e.g. Orville et al., 1966). A series of weaker
286 but clear peaks is also observable at 745, 844, 903, 926, 937, 1012, 1053 and 1131 nm, but
287 with a more variable intensity. The spectra in Figure 5c are compared with a 3- σ noise level
288 (black curve), derived from background fluctuations after the correction described above
289 (Sect.2.1), which is used as a threshold for selecting the most significant emission lines (labeled
290 marks). A list of these lines along with the possible species contributing to them is compiled in
291 Table 2. It is worth noting here that, although the MAJIS instrument implements a powerful
292 embedded despiking algorithm in its acquisition pipeline (Langevin et al., 2020; Poulet et al.,
293 2024), it has not been used in these EGA observations, meaning that the data are affected by
294 several spikes. This circumstance proved favorable in our case, since the despiking processing
295 could have erased or strongly altered lightning signatures. In our case, the coexistence of
296 several emission lines in the same spectrum is the primary factor supporting the interpretation
297 of the observations as lightning emissions, intrinsically transient and localized, rather than
298 ascribing them to spurious instrumental spikes.

299 The largest SNR values, of the order of 20-25, are obtained for the O I 777 nm and N I
300 870 nm lines. As shown in the upper part of Figure 5c, the observed lines overall correlate with
301 those expected from atomic neutral nitrogen and oxygen, once they are calculated at
302 temperatures as high as thousands of kelvin. In this panel, the lines (shown for helping position
303 matching) are modeled on the basis of NIST Atomic Spectra Database (version 5.12, Kramida
304 et al., 2024), at a temperature of 6000 K in Local Thermal Equilibrium (LTE) conditions and then
305 degraded to the MAJIS spectral resolution.

306 It is interesting to note that a faint peak, barely exceeding the 3- σ level, is also observed
307 in MAJIS spectra at 656 nm, coincident with the atomic hydrogen H α , the only line of the Balmer
308 series falling within the MAJIS spectral range (see Sect.4.3 for more details).

309
310



311
 312 **Figure 5 - a)** MAJIS spectra averaged over the lightning pixels of the same frames (A,B,C,D),
 313 in the whole MAJIS spectral range. Emissions diagnostic of lightning are inside the dotted red
 314 box at left, blown up in panel c). The vertical dashed stripe around 2300 nm indicates the
 315 regions of spectral overlap between MAJIS VISNIR and IR channels. **b)** Section of the MAJIS
 316 visible image around lightning pixels (spectral average between 765 and 885 nm), with
 317 lightning frames highlighted by triangles at left. **c)** Lower part: Identification of emission lines
 318 detected in frame-averaged MAJIS lightning spectra. The labels highlight the wavelengths
 319 where the average signal exceeds the 3- σ level above noise (line-filled grey area). Upper part:
 320 Locations of the transitions expected by atomic nitrogen, oxygen and hydrogen, shown as a
 321 normalized intensity calculated in LTE condition at 6000 K (line parameters taken from NIST
 322 Atomic Spectra Database, version 5.12).
 323

324 **Table 2** - Emission lines detected in MAJIS spectra. The atomic transitions most likely
 325 contributing to each line are listed along other possible weaker transitions. The list is compiled
 326 only on the basis of the spectral locations of atomic transitions. Wavelengths in brackets, in
 327 nanometers, indicate the multiplet centers and are taken from the NIST database.

λ MAJIS (nm)	most likely contributions	other possible contributions
656.6	H I (656.3)	N I (660.3); N II (631.3); O II (656.6)
744.5	N I (746.9; 742.2; 743.7; 748.5)	N II (745.1)
777.7	O I (777.3); N I (772.8)	N II (776.2)
822.0	N I (816.6; 821.7); O I (822.2)	
844.3	O I (844.6)	H I (846.7; 843.8; 841.3; 839.2); N II (843.9); O II (837.6)
870.3	N I (868.1; 876.7; 866.4; 865.6)	H I (875.0; 866.5); N II (867.6; 868.7)



903.7	N I (906.1; 902.1; 904.7)	H I (901.5); N II (898.6); O II (900.6)
926.0	O I (926.4; 920.5); N I (918.7)	H I (922.9); O II (928.0); N II (921.7)
937.2	N I (941.9; 939.3; 946.4; 923.2)	N II (921.7; 940.0); O II (938.9)
1011.8	O I (1016.7); N I (1011.3; 1015.5)	
1052.8	N I (1053.9)	N II (1054.1; 1054.7)
1131	O I (1128.6; 1130.2); N I (1129.2)	

328

329

330 **3. Modeling**

331

332 The intensity of the emission lines depends on gas temperature and density within the
 333 lightning discharge channel. Assuming an optically thin LTE plasma, the intensity of an emission
 334 line due to a transition between states $j \rightarrow i$ can be modeled using the Saha equation (see e.g.
 335 Boggs et al., 2021):

$$336 \quad I_{ji} = \beta \frac{g_j A_{ji}}{\lambda_{ji}} e^{-E_j/k_B T} \quad (1)$$

337 where λ_{ji} and A_{ji} are respectively the wavelength and the spontaneous emission Einstein
 338 coefficient of the $j \rightarrow i$ transition, g_j and the E_j are respectively the statistical weight and the
 339 excitation energy of the upper level, k_B is the Boltzmann constant and T the temperature. The
 340 factor $\beta = \gamma h c n_0 / Q(T)$ encloses all the quantities that are wavelength-independent, like the total
 341 number density n_0 of the atomic species and a scaling factor γ related to the observing geometry
 342 (h is the Planck constant, c the light speed and $Q(T)$ the partition function sum of the involved
 343 species).

344 Equation (1) represents the baseline for physically interpreting MAJIS lightning spectral
 345 features. Given that the factor β is independent of the transition, it cancels out in intensity ratios
 346 between lines of the same species.

347 It is important to note that MAJIS was not designed to measure lightning spectra,
 348 particularly in terms of spectral and temporal resolutions. Therefore, further considerations are
 349 presented in the following sections to better determine which quantities can be reliably retrieved
 350 from observations and their associated uncertainties (see sections 3.3 to 3.5).

351

352 **3.1. Line widths and broadening**

353

354 The presence of a rather strong electrical field makes the shape of the spectral lines
 355 emitted in lightning mainly broadened by the Stark effect (e.g. Gosse et al., 2025). In principle,
 356 this fact might offer a way for measuring the electron density in the lightning channel (Uman &
 357 Orville, 1964). However, Stark-broadened FWHMs in lightning are estimated to be $\lesssim 0.3$ nm
 358 (see e.g. Walker & Christian, 2019). Even if most of the emission lines are actually multiplets,
 359 i.e. they are composed of packed Stark-broadened lines slightly shifted with respect to each
 360 other, the expected multiplets width are usually $\lesssim 1$ nm.

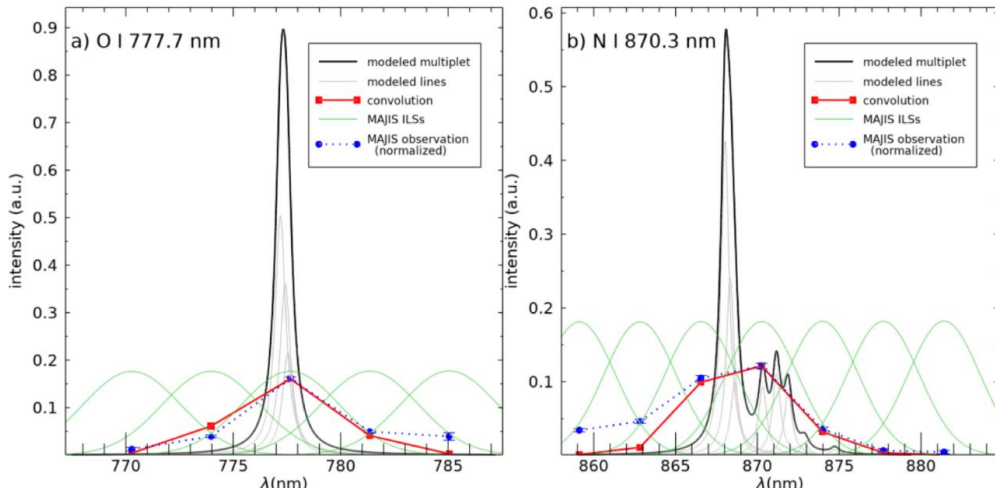
361 In the cube under study, the spectral response of MAJIS pixels (Instrument Line Shape,
 362 ILS) is well described by Gaussian functions (Haffoud et al., 2024), with FWHMs of ~ 5.0 - 5.5 nm
 363 at wavelengths shorter than 1 μ m. On the other hand, the spectral sampling used in the lightning
 364 observations is ~ 3.7 nm, yielding a significant overlap between adjacent spectral bands. In any



365 case, both quantities are larger than expected multiplet widths, which therefore fall well below
 366 the instrumental resolution capability.

367 Nevertheless, some of the stronger lines in MAJIS lightning spectra appear wider than
 368 one spectral point, but this can be readily interpreted as a consequence of the spectral
 369 instrumental sampling. As shown in Figure 6 for the cases of the two strongest lines (O I 777
 370 nm and N I 870 nm), the convolution of a theoretical multiplet spectral shape (black curves),
 371 with the MAJIS ILSSs (green curves) makes the signal appear in distinct spectral points (red
 372 curves). This effect explains the general shape of the observed spectra (blue lines), which is
 373 therefore driven by the instrumental parameters rather than being an indication of a true line
 374 width, confirming that MAJIS observations cannot be used for measuring line broadening (and
 375 therefore electron density).

376



377
 378 **Figure 6 - Effect of the MAJIS spectral response on the shapes of emission lines, for the**
 379 **cases of O I 777 nm line (a) and N I 870 nm line (b). The initial, Stark-broadened, multiplet line**
 380 **(black curve) is modeled as a sum over individual lines (grey curves). Its convolution with**
 381 **MAJIS spectral response (Instrument Line Shapes, ILSSs, shown as dashed green curves)**
 382 **yields a much broader line (red curve), explaining the wider signal seen in MAJIS lightning**
 383 **spectra (blue curves).**

384

385 3.2. Line intensity and spectral filling factors

386

387 MAJIS data have been calibrated in spectral radiance through Instrument Transfer
 388 Function (ITF), which provides the conversion between digital numbers and radiance values
 389 under the assumption that the whole spectral response width of a MAJIS pixel is fulfilled by the
 390 incident light. In the lightning case, dealing with unresolved lines, this standard calibration does
 391 not correctly represent the true emission flux.

392 As a general scheme, we can think the MAJIS spectral radiance in a given band b , I_b ,
 393 characterized by a spectral width of $\Delta\lambda_b$, as the convolution of the source spectral radiance $R(\lambda)$
 394 with the MAJIS ILS $\Phi_b(\lambda)$ of that band:

395
$$I_b = \frac{1}{\Delta\lambda_b} \int_{\Delta\lambda_b} R(\lambda) \Phi_b(\lambda) d\lambda \quad (2)$$



396 where the normalization factor is $\Delta\lambda_b = \int_{\Delta\lambda_b} \Phi_b(\lambda) d\lambda$.
 397 If the source radiance is spectrally constant across the ILS spectral range, $R(\lambda) = R_c$, the
 398 MAJIS calibrated value is rigorous:

$$399 \quad I_b = \frac{1}{\Delta\lambda_b} \int_{\Delta\lambda_b} R_c \Phi_b(\lambda) d\lambda = R_c \quad (3)$$

400 On the contrary, the lightning radiances are emitted in narrow lines, as already discussed in
 401 Sect.3.1. We can think the radiance emitted by the source in a given line k as:

$$402 \quad R_k(\lambda) = R_{k,0} \rho_k(\lambda) \quad (4)$$

403 where the function $\rho_k(\lambda)$ represents a normalized adimensional spectral shape characteristic of
 404 the line k , evaluable *a priori* from line parameters, and $R_{k,0}$ the peak multiplet radiance. In the
 405 case of a multiplet composed of M Stark-broadened Lorentzian lines it will be:

$$406 \quad \rho_k(\lambda) = \frac{1}{\rho_M} \sum_{l=1}^M a_l \frac{w^2}{(\lambda - \lambda_l)^2 + w^2} \quad (5)$$

407 where w is the Stark HWHM, λ_l the central wavelengths of the lines and a_l normalized weights
 408 related to line parameters. The normalization factor ρ_M can be chosen such that $\max(\rho_k) = 1$,
 409 so that the quantity $R_{k,0}$ in equation (4) represents the peak radiance of the multiplet. In any
 410 case, by substituting (4) in (2), we can see that the source spectral radiance is proportional to
 411 the MAJIS calibrated value:

$$412 \quad R_{k,0} = I_b / \delta_{k,b} \quad (6)$$

413 where a spectral filling factor $\delta_{k,b}$ is defined as:

$$414 \quad \delta_{k,b} = \frac{\int \rho_k(\lambda) \Phi_b(\lambda) d\lambda}{\int \Phi_b(\lambda) d\lambda} \quad (7)$$

415 This also allows to retrieve the total radiance (in $\text{W}/\text{m}^2/\text{sr}$) emitted from the line k in the
 416 MAJIS band b as:

$$417 \quad R_{k,tot}(b) = I_b \frac{\int \rho_k(\lambda) d\lambda}{\delta_{k,b}} \quad (8)$$

418

419 The MAJIS filling factors $\delta_{k,b}$ evaluated for the main oxygen and nitrogen lines are
 420 reported in Table 3 and Table 4 respectively, where we can see that most values fall in the
 421 range 0.1-0.3. It is important to stress that such factors depend on both indices k and b , being
 422 referred to the multiplet k viewed in MAJIS band b (adjacent bands can measure the same
 423 multiplet with different filling factors). Furthermore, these correction factors are of course model-
 424 dependent. In particular, they are dependent on the intrinsic line broadening assumed in
 425 modeling multiplets (we adopted a constant value $w = 0.3 \text{ nm}$ for all lines). On the other hand,
 426 the dependence on temperature is mitigated by the fact that the transitions inside the same
 427 multiplet take place between atomic configurations very similar in terms of energy, resulting in
 428 a negligible variation of $\delta_{k,b}$ factors with respect to T .

429

430 3.3. Oxygen lines

431

432 Emission lines diagnostic of atomic oxygen are clearly visible at 777.7 nm and 844.3 nm,
 433 in all MAJIS lightning spectra. A summary of the detected lines is reported in Table 3, including
 434 the values of spectral filling factors defined in the previous Sect.3.2. They are both produced by
 435 oxygen de-excitation through transitions $3p \rightarrow 3s$. The same levels are involved in the emission
 436 at 822 nm, also clearly observable, but not equally diagnostic being it overlapped with a strong
 437 nitrogen line. Another fainter oxygen line is seen at 926 nm, ascribed to $3d \rightarrow 3p$ transitions, that



438 should also contribute to the even fainter feature seen at 1127.5 nm, yet uncertain in nature due
 439 to the closeness of a nitrogen line at 1129 nm.

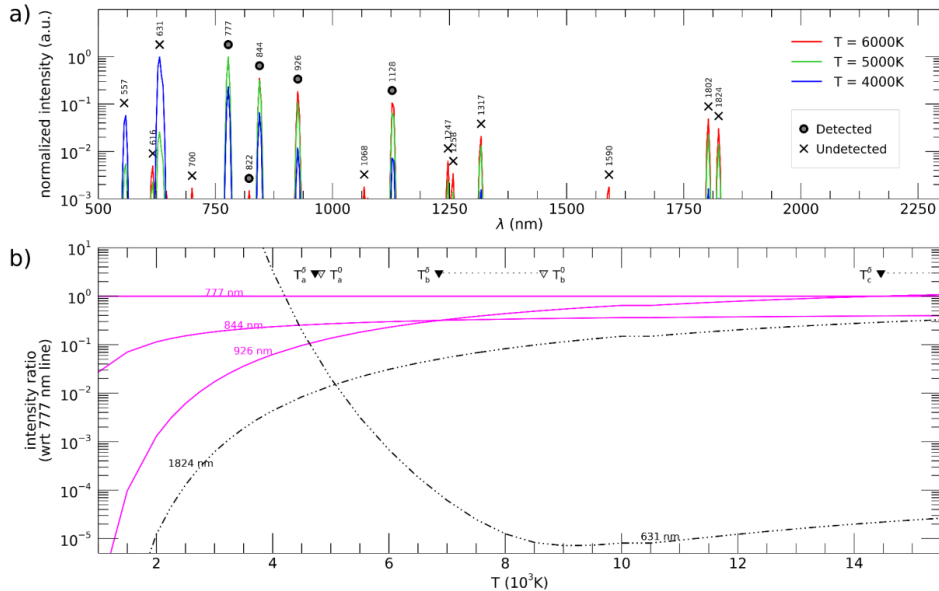
440 In Figure 7a, we can see simulations of the relative intensity of oxygen lines (with respect
 441 to 777 nm line) obtained through equation (1). Temperatures of \sim 5000 K are needed to populate
 442 the 3p and 3d levels enough to produce the observed emissions, but higher temperatures would
 443 increase the population of higher levels (in particular 4s, 4d, 4f, 5d, 5f) yielding stronger
 444 emissions at wavelengths where they are not observed at all (e.g. 616.6, 700.4, 1067.8, 1317.3,
 445 1590.5, 1802.6, 1824.5 nm). On the other hand, a decrease of temperature would make stronger
 446 emissions related to low energy transitions, such the green line at 557.73 nm and the red line
 447 at 630.03 nm (common in auroral phenomena at lower temperature, e.g. Levenko et al., 2019)
 448 that are equally not observed in MAJIS spectra.

449 A comprehensive framework for constraining the temperature is presented in Figure 7b,
 450 where the relative intensities of the most significant emission lines are plotted as a function of
 451 temperature, also accounting for the spectral filling factors discussed in previous Sect.3.2. The
 452 non-detection of the 631 nm line implies its intensity must fall below that of 926 nm line, a
 453 condition that occurs for $T \gtrsim 4700$ K (labeled T_a in the plot). At higher temperatures, the 1824 nm
 454 line is expected to exceed in intensity the 844 nm line (at $T \gtrsim 22000$ K, not shown). Actually, a
 455 stronger upper constraint is provided by the crossing between the 777 nm and 926 nm lines,
 456 that implies $T \lesssim 14000$ K (T_c in the plot) to preserve the dominance of the 777 nm line. As a
 457 consequence, the oxygen line intensities are overall consistent with a broad temperature range
 458 of 4700-14000 K. It is noteworthy that neglecting the spectral filling factor correction would bias
 459 this conclusion, widening the confidence interval to 4800-20000 K (white triangles in Figure 7).
 460

461 **Table 3:** MAJIS emission features identified as O I emission lines. The atomic transition
 462 expected to mainly contribute to the MAJIS line is assigned (from NIST database). The last
 463 column lists their spectral filling factors evaluated through equation (7).

MAJIS λ	associated transitions		δ_{ref}
	nm	nm	
		configurations	
777.7	777.34	2s2.2p3.(4S ^o).3s - 2s2.2p3.(4S ^o).3p [5S ^o -5P]	0.18
822.0	822.20	2s2.2p3.(2D ^o).3s - 2s2.2p3.(2D ^o).3p [3D ^o -3D]	0.27
844.3	844.65	2s2.2p3.(4S ^o).3s - 2s2.2p3.(4S ^o).3p [3S ^o -3P]	0.15
926.0	926.39	2s2.2p3.(4S ^o).3p - 2s2.2p3.(4S ^o).3d [5P-5D ^o]	0.22
1127.5	1128.6	2s2.2p3.(4S ^o).3p - 2s2.2p3.(4S ^o).3d [3P-3D ^o]	0.15

464



465

466 **Figure 7: Calculated intensities for O I lines in the MAJIS VISNIR range at different**
 467 **temperatures, normalized to that of 777 nm line and corrected for spectral filling factor. a)**
 468 **Spectral distribution of strongest O I lines at three temperatures, labeled depending on their**
 469 **detectability in MAJIS spectra. b) Intensity ratios as a function of temperature, for selected O I**
 470 **lines, showing relative changes in a wider range of temperatures. Solid magenta curves**
 471 **represent detected lines, while dot-dashed black curves undetected ones. Significant**
 472 **intersection points are indicated by black-filled triangles: T_a (4730 K) between 631 nm and 926**
 473 **nm, T_b (6860 K) between 926 nm and 844 nm, T_c (13500 K) between 777 nm and 926 nm**
 474 **(white-filled triangles indicate the corresponding values without applying spectral filling factor).**

475

476 3.4. Nitrogen lines

477

478 Neutral atomic nitrogen is responsible for most features in MAJIS spectra as listed in
 479 Table 4. The stronger ones, found in all spectra, are at 745, 822, 870, 937 nm, and are all
 480 associated with transitions $3p \rightarrow 3s$. Other shallower lines are seen peaking at 903, 1012, 1053,
 481 1131 nm, and should be ascribed to N I decay to the $3p$ level ($3d \rightarrow 3p$ and $4s \rightarrow 3p$).

482

483 As in the oxygen's case, a qualitative estimate of a temperature range compatible with
 484 the observations can be inferred by comparing them with model equation (1). Figure 8a,
 485 indicates increasing temperature yields stronger emissions at longer wavelengths, while no
 486 features are seen in MAJIS spectra for $\lambda > 1131$ nm. Although pertaining to the same $3p \rightarrow 3s$
 487 transition, no emission is found at 1353 nm, as well as at 790, 920 and 1073 nm. The same
 488 evidence applies to the missing 1232-1250 nm complex, related to other $3d \rightarrow 3p$ transitions.
 489 Finally, also in this case there are some lower-energy transitions, located near 520 and 1042
 490 nm, whose non-detection can constrain the minimum temperature.

491

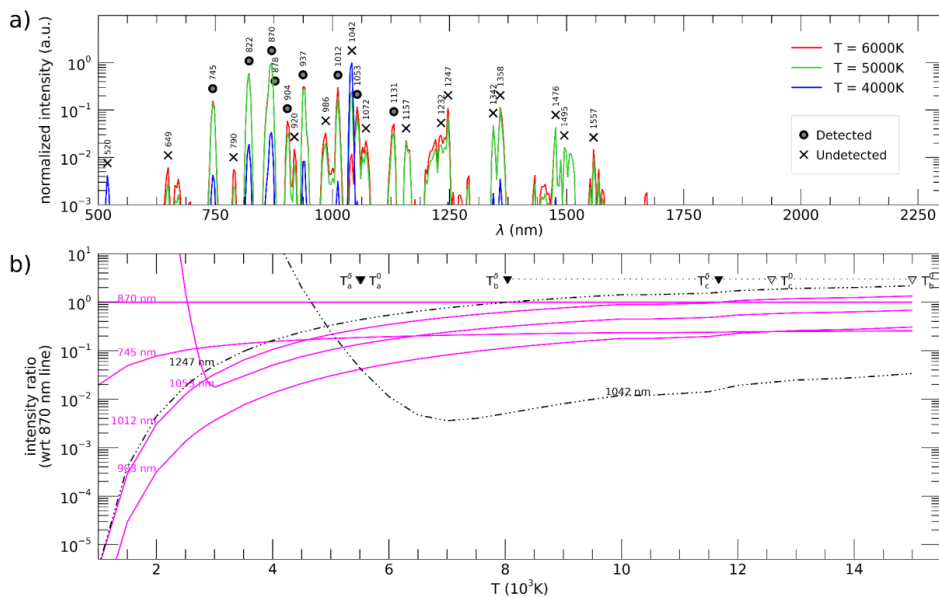
492 As also done for oxygen (see previous Sect.3.3), a temperature plot for nitrogen is shown
 493 in Figure 8b, including trends of relative intensities of most significant nitrogen lines (with
 respect to the 870 nm line). Again, a lower temperature boundary can be determined from the
 crossing of the 903 nm line with the undetected one at 1042 nm (labeled T_a in the plot), yielding



494 $T \gtrsim 5500$ K. Upper boundaries can be inferred from undetected lines at longer wavelengths, such
 495 as the 1247 nm, whose calculated intensity is larger than other detected lines. The crossing
 496 point between the 1247 nm line and the strongest 870 nm (T_b in the plot) would suggest $T \lesssim 8000$
 497 K, but this estimate is highly sensitive to the value of spectral filling factor (shifting to 15000 K if
 498 neglected). A more reliable upper boundary can be set by requiring that the intensity of the 1012
 499 nm line remains below that of 870 nm one, yielding $T \lesssim 12000$ K (T_c in the plot).

500 Hence, on this semiquantitative basis, the range of temperatures compatible with the
 501 nitrogen lines intensities (5500-12000 K) is also compatible with that derived from oxygen in the
 502 previous Sect.3.5 (4700-14000 K).

503



504

505 **Figure 8:** Calculated intensities for N I lines in the MAJIS VISNIR range at different
 506 temperatures, normalized to that of 870 nm line and corrected for spectral filling factor. **a)**
 507 Spectral distribution of strongest N I lines at three temperatures, labeled depending on their
 508 detectability in MAJIS spectra. **b)** Intensity ratios as a function of temperature, for selected N I
 509 lines, showing relative changes in a wider range of temperatures. Solid magenta curves
 510 represent detected lines, dashed orange curves uncertain detections, while dot-dashed black
 511 curves undetected ones. Significant intersection points are indicated by black-filled triangles:
 512 T_a (5520 K) between 903 nm and 1042 nm, T_b (12620 K) between 903 nm and 745 nm, T_c
 513 (11670 K) between 1012 nm and 870 nm (white-filled triangles indicate the corresponding
 514 values without applying spectral filling factor).

515

516

517

518

519

520

521 **Table 4** - N I lines in MAJIS-VISNIR range (source: NIST). Main transitions possibly
 522 contributing to the line are identified by electronic configurations. The last column lists the
 spectral filling factors evaluated through equation (7).



MAJIS λ	associated transitions		$\delta_{\kappa_{\text{pp}}}$
nm	nm	configurations	
745.5	745.22 740.65	2s2.2p2.(3P).3s - 2s2.2p2.(3P).3p [4P-4S°] 2s2.2p2.(3P).3s - 2s2.2p2.(3P).3p [4P-2D°]	0.21 0.26
822	821.18	2s2.2p2.(3P).3s - 2s2.2p2.(3P).3p [4P-4P°]	0.29
862.8	865.95 866.44	2s2.2p2.(3P).3s - 2s2.2p2.(3P).3p [2P - 2P°] 2s2.2p2.(1D).3s - 2s2.2p2.(3P).5p [2D - 2P°]	0.20 0.21
866.5	866.44	2s2.2p2.(3P).3p - 2s2.2p2.(3P).3d [2S° - 2D]	0.15
870.3	869.16	2s2.2p2.(3P).3s - 2s2.2p2.(3P).3p [4P-4D°]	0.21
877.7	876.13	2s2.2p2.(3P).3p - 2s2.2p2.(3P).3d [2S° - 4D]	0.18
903.7	902.07 904.99	2s2.2p2.(3P).3p - 2s2.2p2.(3P).3d [2S° - 4F] 2s2.2p2.(3P).3p - 2s2.2p2.(3P).3d [2S° - 2P]	0.12 0.17
937.2-941.0	936.00 939.53 941.94	2s2.2p2.(1D).3p - 2s.2p4 [2D* - 2D] 2s2.2p2.(3P).3s - 2s2.2p2.(3P).3p [2P-2D°] 2s2.2p2.(3P).3s - 2s2.2p2.(3P).3p [2P - 4S*]	0.15 0.16 0.14
1011.8	1011.68	2s2.2p2.(3P).3p - 2s2.2p2.(3P).3d [4D°-4F]	0.24
1015.5	1011.68	2s2.2p2.(3P).3p - 2s2.2p2.(3P).3d [4D* - 2P]	0.17
1052.8	1052.63	2s2.2p2.(3P).3p - 2s2.2p2.(3P).3d [4P* - 4D]	0.30
1127.5	1125.73	2s2.2p2.(1D).3p - 2s.2p4 [2P* - 2D]	0.12
1131.2	1128.86	2s2.2p2.(3P).3p - 2s2.2p2.(3P).4s [4D* - 4P]	0.23

523

524

525

3.5. Temporal resolution

526

527 As far as time is concerned, individual light pulses, studied in lab triggered lightning,
 528 have been observed to raise to a maximum intensity in time scales of 0.5-1.5 μs , then to
 529 decrease exponentially with a longer decay time τ of the order of 10-100 μs (e.g. Walker &
 530 Christian, 2019; Kieu et al., 2019). Analogous to the spectral case discussed above (Sect.3.2),
 531 the radiance value from the standard MAJIS calibration refers to an integration time ($t_{\text{int}} =$
 532 22 ms) that is possibly much longer, and is therefore not representative of the true radiance
 533 emitted by the source. If we consider the simplest case of a single pulse event with a decay time
 534 τ , of the form:

$$535 \quad R(t) = R_{\text{peak}} e^{-t/\tau} \quad (9)$$

536 the MAJIS radiance, given by the time integration up to t_{int} , will be:

$$537 \quad I_{\text{MAJ}} = R_{\text{peak}} \frac{t_{\text{int}}}{\tau} (1 - e^{-t_{\text{int}}/\tau}) \approx \frac{t_{\text{int}}}{\tau} R_{\text{peak}} \quad (10)$$

538 where last term holds if $\tau \ll t_{\text{int}}$. The peak radiance can therefore be retrieved from MAJIS
 539 values by applying a temporal filling factor δ_t :



540

$$R_{peak} = I_{MAJ} / \delta_t \quad \text{with} \quad \delta_t = \frac{\tau / t_{int}}{1 - e^{-t_{int}/\tau}} \approx \frac{\tau}{t_{int}} \quad (11)$$

541

In this simplified model, no instrument noise has been accounted for, making the signal
542 decay to zero. In a more realistic case, during the integration time the emission does not
543 contribute anymore to the signal after dropping below the noise level, and the expression for
544 R_{peak} changes to:

545

$$R_{peak} = (I_{MAJ} - NESR) / \delta_t \quad (12)$$

546

Anyway, contrary to the spectral filling factor, the evaluation of δ_t is much more difficult
547 since we do not know *a priori* the temporal behaviour of the lightning flash. Decay times for
548 individual lines are provided by some lab measurements of triggered lightning, spanning a large
549 range of values. E.g. Walker & Christian (2019) report values $\tau \sim 140$ μ s for the N I 745 nm line,
550 while much shorter decay time ($\tau \sim 18$ μ s) can be inferred from data in Kieu et al. (2019) for the
551 OI 777 nm line. If these times are considered in equation (11), the resulting peak radiance at
552 745 nm and 777 nm would be 160 and 1200 times larger than MAJIS standard ones,
553 respectively. But lightning flashes are rarely composed of single pulses and they rather consist
554 of clustered sequences of pulses, separated from dozens to hundreds of milliseconds, making
555 the light emission to last as a whole for much longer times (> 100 -200 ms), possibly even larger
556 than the MAJIS integration time (Peterson & Rudlosky, 2019).

557

A second order effect related to the poor temporal resolution can also occur for lines
558 having the same decay time but different strength. In this case, during the integration time the
559 contribution to the signal due to the weaker line drops below that due to background noise earlier
560 in time with respect to a stronger line. Therefore, a different distance from the noise level can
561 bias the lines ratio, and possibly temperature retrievals (see Sect.4.2).

562

These considerations can imply large variations, even by orders of magnitude, in
563 estimating the lightning emission intensity from MAJIS data. In order to better constrain these
564 aspects, we attempted to find detections of the same lightning events from either on-ground
565 stations networks or other satellites, eventually providing independent insights on timing and
566 intensities, but without success (more details on this in Sect.4.4).

567

Given the large amount of uncertainty related to this aspect, a value $\delta_t = 1$ has been
568 used for the radiances previously reported in Figure 7 and Figure 8, while further consequences
569 of temporal resolution will be discussed in Sect.4.2.

570

571 4. Discussion

572

573 4.1. The MAJIS observation in the context of lightning spectroscopy

574

575 After a few pioneering works in the 19th century (e.g. Joule, 1872), the spectroscopy of
576 atmospheric lightning was boosted from the 1960s, when fast slitless spectroscopy enabled the
577 identification of several spectral lines in the UV to visible range in individual flashes (e.g.
578 Salanave et al. 1962, 1964; Krider, 1965; Orville, 1966). These time-resolved observations
579 succeeded in identifying atomic and singly-ionized nitrogen lines, as well as atomic oxygen and
580 hydrogen, and in estimating temperature and electron density in the discharge channel (Prueitt,
581 1963; Krider, 1973; Li et al., 2016; Boggs et al., 2021; Xu et al., 2024). A number of lab
582 experiments reproducing natural lightning conditions (triggered lightning) have also been
583 conducted in the subsequent decades (e.g., Larigalde et al., 1981; Barvir et al., 2004; Li et al.,
584 2016; Carvalho et al., 2018; Walker & Christian, 2019; Kieu et al., 2020), allowing more accurate
585 and controlled studies of the discharge processes. Other observations stressed the production
586 of other chemical species triggered by lightning, such as nitrogen oxides or carbon compounds



587 (Franzblau & Popp, 1989; Jadhav et al., 1996; Langford et al., 2004; Kieu et al., 2021). Overall,
588 most recent investigations increased the relevance of lightning in atmospheric physics and
589 chemistry, by stressing its triggering role for other transient events in the upper atmosphere (like
590 sprites, blue jets, and gamma-ray flashes) and the subsequent non-equilibrium atmospheric
591 chemistry providing a possible source of important greenhouse gases such O₃ or N₂O (see e.g.
592 Gordillo-Vázquez & Pérez-Invernón, 2021, and references therein).

593 Modern spectroscopic techniques enabled lightning observations at frame rates as high
594 as 1 MHz or more, with exposure times as short as 0.5 μ s. Current knowledge assumes peak
595 temperatures of the discharge channel around 40000 K during the first few microseconds of the
596 lightning return stroke, with a spectrum composed of hydrogen from disassociated water and
597 singly/doubly ionized lines of atomic atmospheric constituents (i.e. nitrogen, argon, oxygen).
598 Then, a cooling period follows, reaching temperatures in the 20000 K range tens of
599 microseconds after the onset, and with spectra only consisting of neutral atomic emission lines,
600 followed by a slow decrease of line intensities and temperature until signal disappearance over
601 the course of milliseconds. In the longer cooling phase, molecular reactions involving NO_x can
602 occur, even if some authors report anomalously high NO/NO_x ratios for several minutes
603 (Franzblau & Popp, 1989).

604 All the cited spectroscopic observations of terrestrial lightning have been conducted from
605 the ground. On the other hand, space-based observations dedicated to lightning studies usually
606 rely on large-field imaging in narrow spectral filters, often aimed at the 777 nm O I line in the
607 visible spectrum, like the data provided by LIS (Lightning Imaging Sensor, Christian et al., 2003),
608 ASIM (Atmosphere Space Interaction Monitor, Pérez-Invernón et al., 2022), or GLM
609 (Geostationary Lightning Mapper, Goodman et al., 2013) instruments, to name a few. These
610 datasets are optimal for either global or regional statistical studies, like lightning climatology and
611 flash rates (e.g. Cecil et al., 2014), ratio of cloud-to-ground to intracloud flashes (e.g. Boccippio
612 et al., 2001), their relationship with mixed-phase precipitation (e.g. Petersen et al., 2005), or
613 their link with terrestrial gamma ray flashes (e.g. Barnes et al., 2015; Gjesteland et al., 2017).
614 On the other hand, spectral extensions of space-based observations to the blue/ultraviolet
615 spectral range (like the 180 and 337 nm spectral bands of ASIM) proved useful for improving
616 the physical understanding of blue flashes and elves (Li et al., 2021; Li et al., 2023; Bai et al.,
617 2023; Bjørge-Engeland et al., 2024).

618 Lightning is also of great interest for other planetary atmospheres in the Solar System
619 and beyond, with evidence having been accumulated over the years on many planets (see Aplin
620 & Fischer, 2017, for a review). The first detection on Jupiter dates back to the Voyager 1
621 encounter (Gurnett et al., 1979), followed by confirmations by the Cassini (Dyudina et al., 2004)
622 and Juno (Kolmašová et al., 2018; Brown et al., 2018; Imai et al., 2019; Becker et al., 2020;
623 Kolmašová et al., 2023) spacecrafts. Data from the Voyager probes allowed inference of
624 lightning on the other giant planets, i.e. on Saturn (Warwick et al., 1982, then firmly assessed
625 by Cassini spacecraft, Fischer et al., 2006), on Uranus (Zarka & Pedersen, 1986), and on
626 Neptune (Gurnett et al., 1990). In many of these cases, electrical discharges have been
627 identified thanks to their radio and microwave emissions, and sometimes through visible
628 imaging of possible flashes associated with thick cloud structures. On Venus, preliminary
629 insights of lightning processes were not confirmed by in-depth scrutiny of imaging spectrometry
630 datasets by Venus Express (Cardesín Moinelo et al., 2016), leaving the occurrence of lightning
631 on this planet still debated (Lorenz, 2018). The only evidence of transient luminous events
632 registered by a spectrometer has been reported at Jupiter by the Juno UV spectrograph,
633 although the observed spectra, dominated by H Lyman band emission at 160 nm and hence



634 very similar to Jovian auroral emissions, could be ascribed to events occurring above the Jovian
635 clouds, like sprites or elves (Giles et al., 2020).

636

637 4.2. **Emitted energy**

638

639 The strongest single-pixel intensities registered by MAJIS in lightning spectra are found
640 in the oxygen line at 777 nm (max radiance of $0.418 \text{ W/m}^2/\text{sr}/\mu\text{m}$) and in the nitrogen line at 870
641 nm (max radiance of $0.374 \text{ W/m}^2/\text{sr}/\mu\text{m}$), both within the flash D.

642 As discussed in Sect.3, these radiance values do not represent the emitted source
643 radiance, being biased by resolution effects. Dimensionless filling factors can be introduced to
644 attempt recovering the emitted radiances:

645
$$R_{kb} = I_b / (\delta_s \cdot \delta_{t,kb} \cdot \delta_{\lambda,kb}) \quad (13)$$

646 Here R_{kb} is the radiance emitted in the line k and measured in MAJIS band b , I_b is the
647 MAJIS standard-calibrated radiance, and δ_s , $\delta_{t,kb}$, $\delta_{\lambda,kb}$ are the spatial, temporal and spectral
648 filling factors respectively. However, spatial and temporal filling factors are only relevant if
649 dealing with specific quantities such as radiance, but they are not needed to derive the total
650 energy impinging the detector. As the lightning flashes are the only sources of photons, MAJIS
651 signal is already proportional to the lightning flux integrated over the pixel's footprint and flash
652 duration, and only the spectral filling factor $\delta_{\lambda,kb}$ has to be applied to retrieve the emitted
653 radiance. In other words, by taking advantage of equation (8), if the emission line k is covered
654 by the MAJIS band b , the measured energy density, per unit area and solid angle, is $D_k =$
655 $R_{k,tot}(b) t_{int}$ (in $\text{J/m}^2/\text{sr}$), which is a quantity comparable with other observations being
656 independent on instrumental parameters. In the further assumptions that this energy density is
657 uniform over the whole flash area Σ_f (i.e. the circular regions introduced in Sect.2.2) and that
658 the light of the discharge, isotropically emitted by lightning, is fully backscattered by clouds
659 towards the detector with negligible loss, we can evaluate the total energy E_k emitted by a
660 lightning in the line k as:

661
$$E_k = D_k 4\pi \Sigma_f = R_{k,tot}(b) t_{int} 4\pi \Sigma_f \quad (14)$$

662 The values of D_k and E_k obtained for the strongest lines O I 777 nm and N I 870 nm are
663 summarized in Table 5, associated with statistical uncertainties, of the order of 25%, derived
664 from error propagation of MAJIS uncertainties.

665 The values at 777 nm are particularly useful for comparing MAJIS observations with
666 other datasets, since this line is routinely monitored by satellite observations devoted to
667 lightning. Our derived energy densities are compatible with flash radiances reported in literature
668 for average-intensity lightning. If early airborne observations reported 90% flashes having
669 energy larger than $5 \cdot 10^{-6} \text{ J m}^{-2}\text{sr}^{-1}$ (Christian & Goodman, 1987), modal values obtained from
670 LIS statistics range around $0.5 \text{ J m}^{-2}\text{sr}^{-1}\mu\text{m}^{-1}$ (corresponding to $\sim 5 \cdot 10^{-4} \text{ J m}^{-2}\text{sr}^{-1}$ once a line width
671 of the order of 1 nm is taken into account, see Köhn et al., 2024, their figure 8), which is a value
672 only 5 times higher than those in Table 5. The total energy released through this line ranges
673 between 140 and 700 kJ in MAJIS observations, but if we consider the frames B, C and D as
674 part of a single flash (spanning a total time of 422 ms, not far from the average 345 ms flash
675 duration over ocean, see e.g. Rudlosky et al., 2019), the integrated energy rises to $\sim 1.3 \text{ MJ}$.
676 These values reside near the lower boundary of global statistics, which spans from 1 MJ for
677 small flashes to $> 10 \text{ GJ}$ for superbolts (e.g. Peterson, 2023). Anyway, it is worth keeping in mind
678 that the values we inferred depend on assumptions about areal and angular integration that are
679 not well constrained and the E_k values can represent a lower limit of the actual flash energy.

680



681 **Table 5** - Intensity of main oxygen and nitrogen emissions for the four flashes registered by
 682 MAJIS. I_b is the frame-averaged radiance from the standard calibration pipeline; D_k is the
 683 corresponding energy density, while E_k is the lightning emitted energy under the assumption of
 684 equation (14), extrapolated to a minimal flash area Σ_f . The last row reports the energy estimation
 685 considering B, C, D as pertaining to a unique flash and are obtained by spreading their average
 686 energy density over the largest area of frame D.

flash	Σ_f	OI 777 nm line			NI 870 nm line		
		I_b	D_k	E_k	I_b	D_k	E_k
	km^2	$W \cdot m^{-2} sr^{-1} \mu m^{-1}$	$10^{-5} J \cdot m^{-2} sr^{-1}$	kJ	$W \cdot m^{-2} sr^{-1} \mu m^{-1}$	$10^{-5} J \cdot m^{-2} sr^{-1}$	kJ
A	624	0.07 ± 0.02	8.9 ± 2.2	700 ± 170	0.04 ± 0.01	6.8 ± 2.4	540 ± 180
B	79	0.10 ± 0.02	14.0 ± 3.2	140 ± 30	0.09 ± 0.02	16.0 ± 4.1	160 ± 40
C	113	0.12 ± 0.03	11.0 ± 2.8	160 ± 40	0.06 ± 0.02	12.0 ± 3.5	170 ± 50
D	256	0.12 ± 0.03	16.0 ± 3.5	510 ± 110	0.10 ± 0.02	19.0 ± 4.4	600 ± 140
B + C + D			1330 ± 300				1500 ± 380

687

688

689

4.3. Temperature

690

691 In sections 3.3 and 3.4 we deduced broad ranges of temperatures compatible with
 692 MAJIS lightning observations (corrected for spectral resolution only) from qualitative
 693 considerations on oxygen and nitrogen emissions, appearing in agreement with each other at
 694 least on order of magnitude (4700-14000 K from oxygen, 5100-11700 K from nitrogen). We
 695 investigate here two alternative methods for constraining the temperature in a more quantitative
 696 way.

697

698

4.3.1. Method 1: intra-species line ratios

699

700 If we consider two multiplet transitions $j \rightarrow i$ and $m \rightarrow n$ of the same species, both
 701 described by equation (1), the radiance ratio of the two MAJIS bands covering them, I_b and I_q
 702 respectively, can be expressed as:

$$703 T = \frac{E_m - E_j}{k_B} \left[\ln \left(\frac{\lambda_{ji} g_m A_{mn} \delta_{t,q} \delta_{\lambda,b} I_b}{\lambda_{mn} g_j A_{ji} \delta_{t,b} \delta_{\lambda,b} I_q} \right) \right]^{-1} \quad (15)$$

704 where only the spectral filling factors have been included.

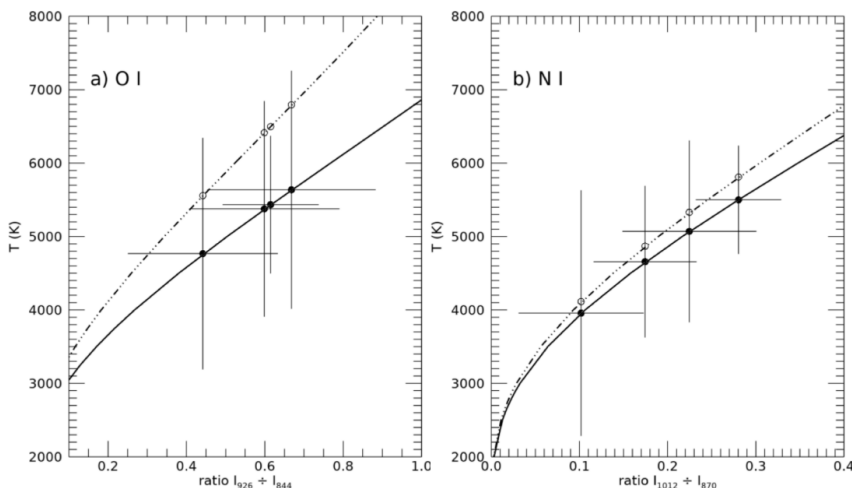
705 This approach is widely adopted for measuring lightning channel temperature when
 706 dealing with spectrally- and temporally-resolved measurements of both natural and triggered
 707 lightning (e.g. Li et al., 2016; Kieu et al., 2021; Boggs et al., 2021). For MAJIS, the application
 708 of this equation is limited to bands covering one single multiplet, hence we selected the 844 nm
 709 and 926 nm lines in the case of oxygen, while the 870 nm and 1012 nm lines were chosen for
 710 nitrogen. Under the assumption that each pair of selected lines shares the same decay time (i.e.



711 $\delta_{t,q}/\delta_{t,b} = 1$), we obtain the results summarized in Figure 9 and Table 6. The associated
 712 uncertainties are largely dominated by MAJIS measurement errors, whereas uncertainties in
 713 the multiplet parameters are considered negligible in this context.

714 All the obtained temperatures are rather similar, given also the high uncertainty levels
 715 ($\sim 20\text{-}30\%$). Those retrieved from nitrogen (4800 ± 1200 K on average) are systematically lower
 716 by a small amount ($\sim 2\text{-}15\%$, not statistically significant) than those from oxygen (5300 ± 1400 K
 717 on average). In the same Figure 9 the effect of spectral resolution is also shown (dash-dotted
 718 curve), revealing that the temperatures retrieved without correction are systematically higher.
 719 The effect is more pronounced in the oxygen case (usually characterized by narrower multiplets)
 720 where it amounts to $\sim 20\%$ (lower than 5% for nitrogen), but still small with respect to
 721 uncertainties.

722



723

724 **Figure 9**- Lightning channel temperatures for the 4 MAJIS flashes, retrieved from the ratios of
 725 lines 926 nm and 844 nm for oxygen (panel a) and 1012 nm and 870 nm for nitrogen (panel
 726 b). Solid points with error bars show the retrieved values accounting for the spectral filling
 727 factor correction, whose temperature values are reported in Table 6. White points on the dash-
 728 dotted curve refer to the uncorrected MAJIS radiance values.

729

730 In any case, MAJIS observations suggest lightning channel temperatures of the order of
 731 5000 K, on the lower edge of the range of temperatures for natural lightning reported in literature.
 732 For example, temperatures up to 15000-25000 K are found by Boggs et al. (2021) by using the
 733 ratio of oxygen lines at 777 nm and 716 nm (undetected by MAJIS). Temperatures up to 30000
 734 K were derived from observations of ionized nitrogen emissions (Orville, 1968), known to last
 735 for even shorter times at the beginning of a flash. Anyway, lightning channel temperature is
 736 related to its electrical current (Li et al., 2016), and colder events can occur on the top of the
 737 cloud, like streamer-like discharges and narrow bipolar events (Liu et al., 2021). Even if such
 738 events do not show evidence of emission at 777 nm, we cannot exclude that MAJIS
 739 observations encompassed different types of transient luminous events at different
 740 temperatures, further altering the ratios of observed line intensities.

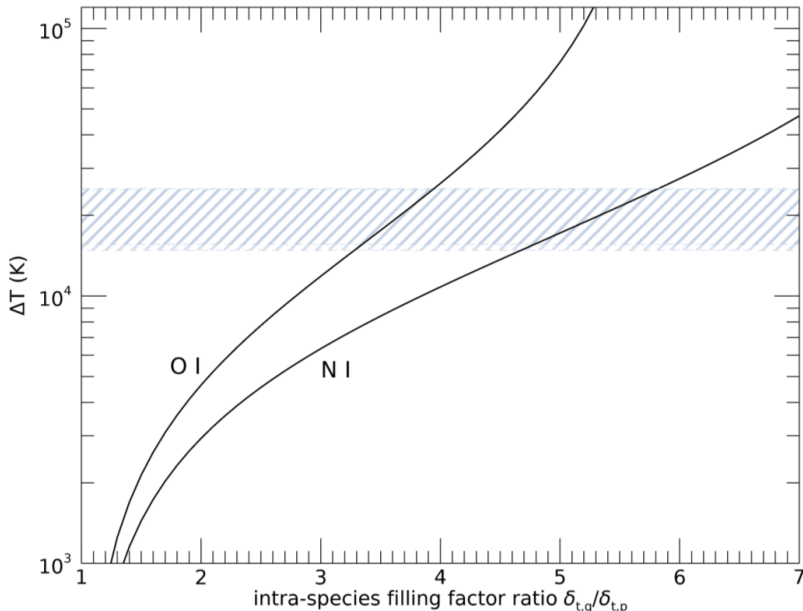
741

742 A possible source of bias in our temperature estimation may be related to the uncertainty
 743 on the ratio of temporal filling factors $\delta_{t,q}/\delta_{t,b}$ in both oxygen and nitrogen cases. The inverse
 log dependence of the temperature on this ratio in equation (15) makes the retrieval very



744 sensitive to this poorly constrained quantity. This sensitivity is represented in Figure 10, where
 745 the large offset of temperatures resulting from rather small variation of $\delta_{t,q}/\delta_{t,b}$ can be
 746 appreciated for both oxygen and nitrogen cases.

747



748

749 **Figure 10-** Sensitivity of the temperature derived from equation (15) to the ratio of temporal
 750 filling factors, for both oxygen and nitrogen cases (same emission lines of Figure 9). Y axis
 751 represents the offset of temperature with respect to the case $\delta_{t,q}/\delta_{t,b} = 1$. Line-filled area
 752 indicates the offset range needed to match the temperatures from method 2 (inter-species
 753 ratios, see Sect. 4.2.2).

754

755 4.3.2. Method 2: inter-species (oxygen to nitrogen) line ratio

756

757 Another way to infer lightning temperature involves modeling the intensity ratios of
 758 oxygen lines with respect to the nitrogen ones. In this case, the β factor in equation (1) does not
 759 cancel out, and the ratio of the number densities and partition function sums have to be treated
 760 explicitly. If we assign the $j \rightarrow i$ transition to an oxygen line (e.g. at 777 nm) and the $m \rightarrow n$ to a
 761 nitrogen line (e.g. 870 nm), we can keep the same notation of (15) and solve for the number
 762 density ratio to have:

$$763 \frac{n_O}{n_N} = \frac{I_b(O)}{I_q(N)} \frac{\delta_{\lambda,q}}{\delta_{\lambda,b}} \frac{g_j A_{ji}}{g_m A_{mn}} \frac{\lambda_{mn}}{\lambda_{ji}} \frac{Q_O(T)}{Q_N(T)} e^{\frac{E_m - E_j}{kT}} \quad (16)$$

764

765 In the Earth's atmosphere, atomic nitrogen and oxygen are dissociation products of
 766 molecular N₂ and O₂, the most abundant and stably mixed molecules. Further contribution to
 767 oxygen can also come from H₂O dissociation. The ratio of atomic abundances can therefore be
 768 derived by evaluating the relative dissociation of these molecules at a given temperature.
 769 Including both O₂ and water dissociation, we can write:



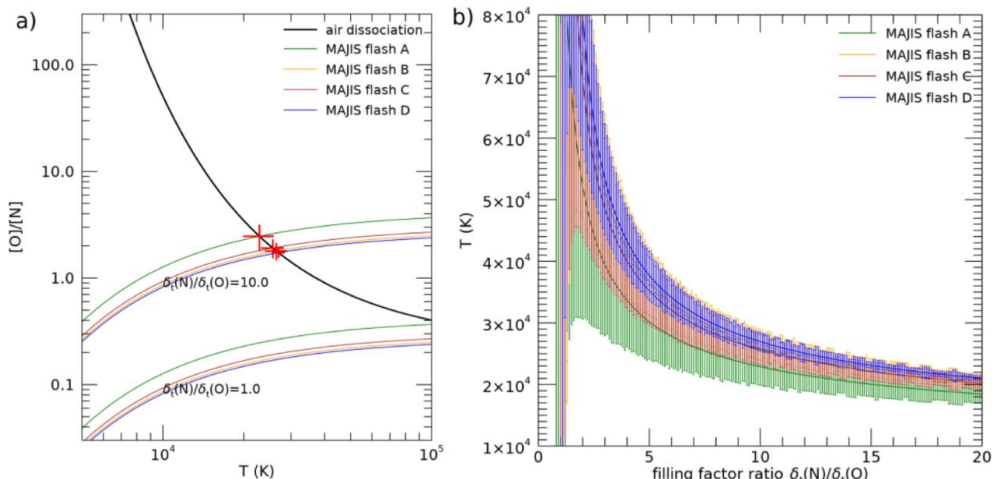
770
$$\frac{n_O}{n_N} = \chi_{O2} e^{\frac{D_{N2}-D_{O2}}{k_B T}} + \frac{1}{2} \chi_{H2O} e^{\frac{D_{N2}-D_{H2O}}{k_B T}} \quad (17)$$

771 where $\chi_{O2} = n_{O2}/n_{N2}$ and $\chi_{H2O} = n_{H2O}/n_{N2}$ represent the molecular mixing ratios, while D_{N2} ,
 772 D_{O2} , D_{H2O} their dissociation energy. This equation provides a theoretical argument to be
 773 compared with the ratio derived from MAJIS observations in equation (16).

774 By evaluating equation (17) with $\chi_{O2}=0.21$, $\chi_{H2O}=0.05$, $D_{N2}=945$ kJ/mol, $D_{O2}=498$
 775 kJ/mol, $D_{H2O}=498$ kJ/mol yields the black curve in Figure 11a. This curve has to be compared
 776 with the ratio obtained through equation (16) by MAJIS data, shown in the same figure. In the
 777 calculation, a ratio of partition functions $Q_O(T)/Q_N(T) = 4$ is assumed, constant in the
 778 temperature range of interest, while line parameters are still taken from the NIST database.

779 The intensity ratio in equation (16) implies the presence of the temporal filling factor ratio,
 780 $\delta_t(N)/\delta_t(O)$, whose value cannot be easily constrained. If we let it as a free parameter, equation
 781 (16) provides a family of curves, as shown in Figure 11a for two values of $\delta_t(N)/\delta_t(O)$. Then,
 782 by solving for temperature (by equating (16) and (17)) we obtain a family of solutions for each
 783 flash detected, illustrated in Figure 11b (error bars are derived from propagation of the MAJIS
 784 radiance uncertainties). We can see that, whatever is the value of $\delta_t(N)/\delta_t(O)$, higher
 785 temperatures are retrieved, always larger than ~ 20000 K. By assuming an educated guess on
 786 decay times of ~ 18 μ s (from Kieu et al., 2019) and ~ 140 μ s (from Walker & Christian, 2019) for
 787 OI and NI respectively, we provide in Table 6 the temperature for a value $\delta_t(N)/\delta_t(O)=10$.

788



789

790 **Figure 11** - Lightning temperature inferred from O/N atomic density ratio. Panel a): the
 791 molecular dissociation model of equation (17) is shown as a black curve, while in colors are
 792 represented the families of curves inferred from MAJIS data with equation (16) with different
 793 ratio of temporal filling factors $\delta_t(N)/\delta_t(O)$. Red crosses indicate the solutions for the
 794 temperature, given by the curves' intersections. Panel b): Families of solution for temperature
 795 retrieved from MAJIS density ratios as a function of filling factor ratio.

796

797

798

799

800



801 **Table 6** - Comparison of lightning temperatures retrieved with different methods. Values in the
802 last column refer to a ratio of temporal filling factors $\delta_t(\text{NI})/\delta_t(\text{OI}) = 10$.

flash	T (K)		
	method 1 (Sect.4.3.1)		method 2 (Sect.4.3.2)
	OI(844nm) / OI(926nm)	NI(870nm) / NI(1012nm)	OI(777nm) / NI(870nm)
A	4800 \pm 1600	4000 \pm 1700	23000 \pm 3000
B	5400 \pm 1500	4700 \pm 1000	26500 \pm 2500
C	5600 \pm 1600	5100 \pm 1200	25700 \pm 2500
D	5400 \pm 900	5500 \pm 700	27000 \pm 1500

803
804 **4.3.3. Comparison between methods**
805

806 It is evident that the two methods investigated do not fully agree with each other on the
807 resulting lightning temperature. The ratio of temporal filling factors $\delta_{t,q}/\delta_{t,b}$ can play a key role
808 in explaining such discrepancies since its values are poorly constrained and the results are quite
809 sensitive to it. In both methods, line ratioing removes any dependence on the number of flashes
810 encompassed by a single measurement. However, lines used in method 1 (of the same species)
811 are of different intensity and are subject to bias due to the different distance from the noise level
812 (see Sect.3.5). Lines used in method 2 are instead of similar intensity (the strongest one for
813 both oxygen and nitrogen) but affected by uncertainty of temporal filling factors ratio. Results of
814 method 2 are closer to those found in literature for peak temperatures of intra-cloud lightning
815 (see Sect.4.1), even if events generated by smaller electrical current are intrinsically colder (Liu
816 et al., 2021). Actually, in order to assess which method is closer to the real temperatures, we
817 should better understand the nature of the observed event and its unresolved characteristics
818 (Sect.4.4). In any case, we can note that, as stressed in Figure 10, intra-species ratios $\delta_{t,q}/\delta_{t,b}$
819 of the order of 3.5 (for oxygen) and 5.5 (for nitrogen) would be sufficient to reconcile the results
820 from method 1 to those of method 2.

821
822 **4.4. Signatures of other species**
823

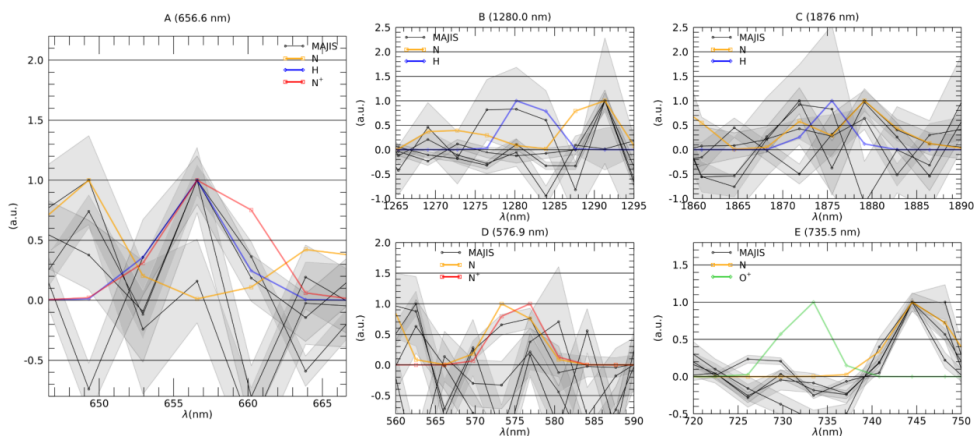
824 Observations of ionized atomic emissions are often reported in the early phases of
825 lightning processes, mainly due to N^+ , O^+ , N^{++} , O^{++} (Kieu et al., 2021). The best diagnostic
826 features of these species fall at wavelengths shorter than those accessible by MAJIS, that might
827 only cover their weaker lines taking place longwards of 500 nm.

828 The only significant signature present in almost all MAJIS spectra that is possibly not
829 due to nitrogen or oxygen is found at 656.6 nm, as highlighted in Figure 12a. where the four
830 MAJIS lightning spectra are shown in black along with their uncertainties. This wavelength
831 encompasses the $\text{H}\alpha$ emission (656.3 nm, blue curve) which, besides being a minor component
832 of non-LTE diffuse terrestrial exosphere emissions (e.g. Larigaldie et al., 1981), is also known



833 to be produced in natural lightning flashes, where it can be efficiently exploited for measuring
834 electron density (Uman & Orville, 1964).

835 However, N^+ also emits at that wavelength, with a slightly different line width (red curve).
836 Both species have other weaker lines at longer wavelengths, N^+ at 575 nm and H at 1280 and
837 1876 nm, that can be used for discrimination. As shown in the other panels of Figure 12, the
838 level of noise prevents a clear detection, even if some of the MAJIS spectral shapes are slightly
839 more correlated with H emissions rather than N^+ . Anyway, although the presence of a 656 nm
840 peak is clear, observations are not conclusive on the nature of the emitter.



841
842 **Figure 12:** Comparison of MAJIS spectral shapes (frame-averaged spectra) with modeled
843 emissions at 6000 K in selected ranges. In order to highlight possible correlations in shape, all
844 spectra are continuum-removed and normalized to unity in the shown spectral ranges.
845 Positive correlation only in panel A for the 656.6 nm feature with either H and N^+ emission.
846

847 A search for other small signatures has been performed without success, as in the case
848 of O^+ shown in Figure 12E.

849 In principle, MAJIS spectra in the thermal range cover several absorption bands of NO_x
850 molecules, whose production is known to be enhanced by lightning activity (LNO_x molecules,
851 see e.g. Schumann & Huntrieser, 2007). Opacity of thunderclouds can strongly affect the
852 retrieval of NO_x (Beirle et al., 2019), but convection can transport NO_x released near the surface
853 to the upper troposphere, where it is mixed with freshly produced LNO_x making detection from
854 space possible. Even if MAJIS data may offer a further chance to check the LNO_x production
855 mechanism, their absorption bands in the IR are strongly overlapped with H_2O ones, and even
856 a qualitative analysis requires a complete modeling of atmospheric thermal emission which is
857 beyond the purpose of the present work.

858

859 4.5. Search for independent lightning detection

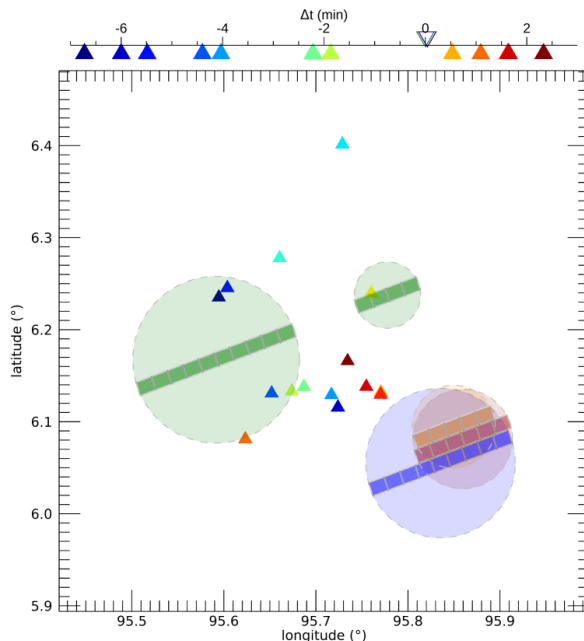
860

861 We have inspected the lists of detections provided by World Wide Lightning Location
862 Network (WWLLN, Hutchins et al., 2012), the Earth Networks Total Lightning Network (ENTLN,
863 (Zhu et al., 2017) and the lightning system operated by the University of Hokkaido (Narita et al.,
864 2018). As illustrated in Figure 13, a sequence of ENTLN strokes is found in the proximity of the
865 MAJIS detection, nevertheless within a few minutes before and after the MAJIS flashes,
866 indicating an active lightning area. The location of some strokes fall within the area of the first
867 MAJIS flash, but they took place ~5 min before the MAJIS observation.



868 This negative result is not surprising, as all lightning location systems mentioned above
869 are most sensitive to lightning return strokes. The return stroke lightning channels are several
870 kilometers long and thus emit the electromagnetic signals in kHz frequencies, which can travel
871 thousands of km in the waveguide formed by the surface of Earth and the bottom of the
872 ionosphere. Such signals received at several network stations are used for the localization of
873 lightning discharges by the time-of-flight method. The lightning events observed by MAJIS were
874 clearly located at the cloud tops and could be associated with high-altitude in-cloud lightning
875 phenomena as leaders, dart-leaders or streamer-like Compact Intracloud Discharges also
876 called Narrow Bipolar Events (Petersen & Beasley, 2013; Kolmašová et al., 2023; Nag et al.,
877 2010; Liu et al., 2021; see also Rakov and Uman, 2007 for an overview on different lightning
878 phenomena). Unfortunately, the area of interest is not covered by any geostationary lightning
879 imager, which could prove a lightning activity at the cloud tops.

880 Incidentally, it is worth noting that wavy structures possibly linked to thunderstorm events
881 are observed in MAJIS images acquired during the same EGA campaign (see Oliva et al., 2025,
882 this issue) and pointing to areas adjacent to that discussed in this work, further testifying to the
883 existence of intense thunderstorm activity in the area observed by MAJIS during the EGA.



884
885 **Figure 13:** Locations and timing of strokes detected by searched ground networks (triangles)
886 with respect to MAJIS observations (shaded circles). Time differences of ground networks'
887 strokes with respect to MAJIS are indicated in the upper axis.
888
889

890 4.6. Extrapolation to lightning detection in Jupiter's atmosphere

891
892 This serendipitous observation during the very brief Earth flyby suggests that a similar
893 opportunity could arise at Jupiter, one of the primary targets of the JUICE mission.



894 On Earth, the lightning flash rate is highly variable in space and time (e.g. Blakeslee et al., 2020).
895 The Sumatra region is one of the areas where the flash rate is higher, quantifiable during
896 summer in ~ 30 flashes·km $^{-2}$ ·yr $^{-1}$ ($\sim 10^{-6}$ flashes·km $^{-2}$ ·s $^{-1}$). This made the first cube of the EGA
897 sequence the most likely to capture lightning. Taking into account the spatial and temporal
898 coverages detailed in Sect.2.1, this flash rate yields a probability of a lightning detection during
899 this cube's acquisition of $\sim 0.6\%$.

900 On Jupiter, lightning is also thought to be triggered by moist convective processes within
901 water cloud layers, at pressure levels of a few bars. Galileo spacecraft recorded good statistics
902 of optical flashes associated with lightning storms, with energy release estimated as high as
903 ~ 10 GJ (Little et al., 1999; Gierasch et al., 2000), while New Horizons spacecraft detected some
904 lightning activity at polar latitudes as well (Baines et al., 2007). These optical observations, all
905 relying on nightside imaging, suggested flash rates lower than on Earth, around 0.004
906 flashes·km $^{-2}$ ·yr $^{-1}$, raised to ~ 0.07 flashes·km $^{-2}$ ·yr $^{-1}$ by Galileo probe dedicated analyses (Rinnert
907 et al., 1998). However, more recent observations by Juno, based on microwave measurements,
908 found on Jupiter a lightning rate comparable to Earth's one, ~ 1 - 30 strokes·km $^{-2}$ ·yr $^{-1}$ (Kolmašová
909 et al., 2018). By considering a typical resolution of ~ 150 km/pixel and an integration time of 0.1
910 s, these latter values translate to a probability of a lightning event in a single MAJIS pixel at
911 Jupiter around 0.07-1%. If the discrepancy in flash rate between optical and microwave
912 observations is not sample-biased but is due to different atmospheric opacity, then the lower
913 flash rates have to be assumed for MAJIS, lowering the detection probability per pixel to 10^{-6} .
914 From the spectral point of view, since the composition of the Jovian atmosphere is very different
915 from that of Earth, a possible detection of lightning should rely on totally different spectral
916 signatures. To estimate the most likely emission lines detectable by MAJIS, we considered a
917 unique gaseous layer with a standard Jovian atmosphere composition (populated by H₂, He,
918 H₂O, CH₄, NH₃, Ne, H₂S, Ar, Kr, Xe, with fixed mixing ratios 0.84, 0.16, 1.5e-3, 1.8e-4, 1.9e-4,
919 3.1e-5, 6.1e-6, 1.5e-9, 7e-11 respectively), then we evaluated the abundances of their
920 dissociation products by using the simplified model of equation (17). Dissociation energies are
921 set to the following values: D(O₂)=498 kJ/mol, D(H₂)=431 kJ/mol, D(CH₄→H+CH₃)=463.1
922 kJ/mol, D(CH₃→CH₂+H)=463.1 kJ/mol, D(CH₂→CH+H)=422.6 kJ/mol, D(CH→C+H)=338.7
923 kJ/mol, D(H₂O)=497.3 kJ/mol (Ruscic, 2015), D(NH₃→NH₂+H)=3226 cm $^{-1}$ (McCarthy et al.,
924 1987), D(H₂S→H₂+S)=0.2 eV/mol (Gutsol et al., 2010). Finally the ratios of atomic abundances
925 are used to estimate the relative intensities of potential lightning emission. Results of the
926 calculation are shown in Table 7, for a lightning temperature of 1000 K.

927 It is not surprising that hydrogen would dominate Jovian lightning spectra, being by far the most
928 abundant species. The strongest line is the H α , but several other hydrogen lines could reach a
929 significant intensity. Most of the lightning energy ($> 60\%$ of the total) should escape through the
930 649-660 nm wavelength range, but a significant energy flux ($\sim 30\%$) may occur through the
931 1871-1879 nm window. Secondary but still possibly relevant ranges are 1280-1284 nm and
932 1090-1094 nm ($\sim 5\%$ and $\sim 1\%$ of the total energy respectively).

933 The only other species reaching a comparable level of intensity within the MAJIS spectral range
934 is sulphur, whose line at 922.3 nm could reach 1% intensity of the H α . All other atomic species
935 are confined at lower intensities, starting from the oxygen line at 777 nm expected to reach a
936 0.08% level.

937 For a more comprehensive simulation of the MAJIS signal from Jovian lightning, both
938 instrumental response and scattering/absorbing spectral properties of overlying cloud layers
939 have to be taken into account. For instance, the instrumental NESR derived by background
940 fluctuations (see Figure 2b) can be slightly larger near 650 nm than near 1870 nm, partially
941 compensating the relative detection probability mentioned above. On the other hand, emission



942 lines located inside strong methane absorption bands may have an enhanced detection
943 probability due to reduced scattered light, increasing their visibility on the planet's dayside as
944 well (as recently reported by JunoCam analyses, Fletcher et al., 2025, in press). The full setting
945 of instrumental parameters will be also crucial for optimizing both the probability of detection
946 and interpretation of lightning events, and will be better assessed in future planning. Also, a
947 quantitative estimation of SNR requirements, that would require more complex models to
948 calculate the absolute abundances of potential emitters, is beyond the purpose of this work.

949 In case of detection, lightning temperature retrievals in Jupiter's case should rely solely
950 on method 1 (Sect. 4.2.1), being signatures of species other than hydrogen unlikely. In this
951 context, the coverage of both 650 nm and 1870 nm spectral ranges is effective for constraining
952 temperature, as they probe a suitable variety of electronic level populations. However, issues
953 related to spatially and temporally unresolved measurements will hold also in the jovian case,
954 and a more accurate de-biasing, based on detailed models of atmospheric and instrumental
955 processes, will be desirable.

956
957 **Table 7- Modeled ratios of line intensities for lightning emissions in Jupiter's atmosphere,**
958 *relative to the H α line, for a lightning temperature of 1000 K.*

multiplet	line ratio	multiplet	line ratio	multiplet	line ratio
H α (656.6 nm)	100%	H (1879.2 nm)	7%	H (1944.8 nm)	1%
H (1875.5 nm)	57%	H (1283.9 nm)	6%	H (1004.3 nm)	1%
H (652.9 nm)	36%	H (1093.9 nm)	4%	H (1090.2 nm)	1%
H (660.2 nm)	24%	H (2164.6 nm)	1%	H (1997.6 nm)	1%
H (1871.9 nm)	14%	H (649.3 nm)	1%	S (922.3 nm)	0.74%
H (1280.2 nm)	8%	H (2168.3 nm)	1%	O (777.7 nm)	0.08%

959
960 **5. Summary and conclusion**
961
962 The data acquired by MAJIS during the JUICE Earth Gravity Assist maneuver on 2024,
963 Aug, 20th, revealed a serendipitous detection of lightning emissions, taking place at nighttime
964 near Sumatra island. The detection consists of a few spectra in the visible range showing
965 emission lines diagnostic of neutral atomic oxygen and nitrogen. Oxygen is clearly identified by
966 the 777 nm line, routinely used in monitoring lightning activity by satellite, whereas nitrogen
967 strongest emissions take place at 870 nm and 822 nm. An emission is also found at 656.6 nm,
968 even though we cannot conclusively discriminate between contributions by H or N⁺. The
969 observed four flashes can be localized near the edge of a thick thunderstorm cloud, but we did
970 not find any independent detection of the same events neither by ground-based lightning
971 networks nor by satellites.

972 Although the characteristics of MAJIS observations are not optimal for measuring such
973 extreme phenomena, we attempt to model the MAJIS emission spectra in order to retrieve as
974 much physical information as possible. In particular, MAJIS could not resolve the lightning flash
975 features either spectrally or temporally, raising the need for specific corrections to the standard
976 calibrated spectral radiance values, quantified where possible through spectral and temporal



977 filling factors. Under these assumptions, we estimate the flashes emitted through the 777 nm
978 oxygen line an energy of 140-700 kJ, and up to 1.3 MJ for the event considered as a whole.

979 The relative intensity of emission lines is a well-known proxy for measuring the
980 temperature of the lightning channel. We attempt to apply this method to both ratios of oxygen
981 lines and nitrogen lines, but the obtained temperatures, ranging between 4000 and 5600 K, with
982 uncertainties of the order of 30%, appear well below the peak temperatures of intra-cloud
983 lightning reported in literature (20000-35000 K), but compatible with colder phenomena like
984 streamer-like discharges and narrow bipolar events (Liu et al., 2021).

985 An alternative approach for temperature retrieval from ratios of oxygen to nitrogen lines
986 has also been attempted. In this case much higher values are retrieved, around 23000-27000
987 K, closer to the highest peak temperature values. Both methods can yield temperatures biased
988 by our incomplete knowledge of the temporal trend of individual lines within the lightning flashes.
989 A more robust assessment in this regard is not possible without independent knowledge of the
990 nature and unresolved characteristics of the event, since the MAJIS observation could have
991 registered different types of transient luminous events occurring in short times at different
992 temperatures.

993 The EGA data here discussed represent the first ones acquired by MAJIS on a planetary
994 target. From this point of view, the analysis demonstrates the valuable performances of the
995 instrument also on an unexpected finding. This is also true in the case of Jupiter's atmosphere,
996 a primary target of the JUICE mission. Considering also that Jupiter's atmosphere is thought to
997 host a lightning rate as high as on Earth (Kolmašová et al., 2018), repeated MAJIS observations
998 of the Jovian night hemisphere have a non-zero chance to capture lightning flash spectra.
999 Hence, this work is also intended to help planning and analysis of future Jupiter observations.

1000
1001 **Code availability** - Simple scripts have been developed for data management and processing
1002 and for the implementation of the models described to MAJIS data. The codes will not be
1003 published but can be shared upon private request to the corresponding author.

1004
1005 **Data availability** - The MAJIS data acquired during the JUICE Moon–Earth flyby in August 2024
1006 are currently under the mission's cruise-phase proprietary period. These data will be made
1007 available through the ESA Planetary Science Archive following the first Cruise Archive Delivery,
1008 which is currently scheduled for six months after Earth Gravity Assist #3 in 2029.

1009
1010 **Author contribution** - ED carried out lightning data identification and processing, ED and FO
1011 developed data analysis, interpretation, and manuscript preparation, with significant
1012 contributions by FP, GP, AM, LF. IK performed ground-based lightning counterparts search,
1013 while FP, GP, YL, GF, SR, BS provided calibrated MAJIS data. All coauthors contributed to
1014 discussing the results and writing the manuscript.

1015
1016 **Competing interests** - The authors declare that they have no conflict of interest.

1017
1018 **Acknowledgments**

1019
1020 JUICE is a mission under ESA leadership with contributions from its Member States,
1021 NASA, JAXA and the Israel Space Agency. It is the first Large-class mission in ESA's Cosmic
1022 Vision programme.



1023 The Italian participation in the JUICE mission is funded by the Italian Space Agency
1024 (ASI). In particular, this work has been developed under the ASI-INAF agreement n. 2023-6-
1025 HH.0.

1026

1027 References

1028

1029 Acton, C., Bachman, N., Semenov, B., & Wright, E. (2018). A look towards the future in the
1030 handling of space science mission geometry. *Planetary and Space Science*, 150, 9–
1031 12. <https://doi.org/10.1016/j.pss.2017.02.013>

1032 Acton, C. H., Jr. (1996). Ancillary data services of NASA's Navigation and Ancillary
1033 Information Facility. *Planetary and Space Science*, 44(1), 65–70.
[https://doi.org/10.1016/0032-0633\(95\)00107-7](https://doi.org/10.1016/0032-0633(95)00107-7)

1034 Aplin, K. L., & Fischer, G. (2017). Lightning detection in planetary atmospheres. *Weather*,
1035 72(2), 46–50. <https://doi.org/10.1002/wea.2817>

1036 Bai, X., Füllekrug, M., Chanrion, O., Soula, S., Peverell, A., Mashao, D., Kosch, M., Husbjerg,
1037 L., Østgaard, N., Neubert, T., & Reglero, V. (2023). Height determination of a blue
1038 discharge observed by ASIM/MMIA on the International Space Station. *Journal of
1039 Geophysical Research: Atmospheres*, 128(7). <https://doi.org/10.1029/2022jd037460>

1040 Barnes, D. E., Splitt, M. E., Dwyer, J. R., Lazarus, S., Smith, D. M., & Rassoul, H. K. (2015). A
1041 study of thunderstorm microphysical properties and lightning flash counts associated
1042 with terrestrial gamma-ray flashes. *Journal of Geophysical Research: Atmospheres*,
1043 120(8), 3453–3464. <https://doi.org/10.1002/2014jd021495>

1044 Barvir, P., Kubes, P., Krawarik, J., Scholz, M., Karpinski, L., Sadowska-Skladnik, E., &
1045 Malinowski, K. (2004). Research of the discharge with parameters of lightning channel.
1046 *Czechoslovak Journal of Physics*, 54(S3), C274–C278.
<https://doi.org/10.1007/bf03166412>

1047 Becker, H. N., Alexander, J. W., Atreya, S. K., Bolton, S. J., Brennan, M. J., Brown, S. T.,
1048 Guillaume, A., Guillot, T., Ingersoll, A. P., Levin, S. M., Lunine, J. I., Aglyamov, Y. S., &
1049 Steffes, P. G. (2020). Small lightning flashes from shallow electrical storms on Jupiter.
1050 *Nature*, 584(7819), 55–58. <https://doi.org/10.1038/s41586-020-2532-1>

1051 Beirle, S., Borger, C., Dörner, S., Li, A., Hu, Z., Liu, F., Wang, Y., & Wagner, T. (2019).
1052 Pinpointing nitrogen oxide emissions from space. *Science Advances*, 5(11).
<https://doi.org/10.1126/sciadv.aax9800>

1053 Bjørge-Engeland, I., Østgaard, N., Marisaldi, M., Luque, A., Mezentsev, A., Lehtinen, N.,
1054 Chanrion, O., Fuglestad, A. N., Neubert, T., & Gordillo-Vazquez, F. J. (2024). High
1055 peak current lightning and the production of elves. *Journal of Geophysical Research:
1056 Atmospheres*, 129(4). <https://doi.org/10.1029/2023jd039849>

1057 Blakeslee, R. J., Lang, T. J., Koshak, W. J., Buechler, D., Gatlin, P., Mach, D. M., Stano, G.,
1058 T., Virts, K. S., Walker, T. D., Cecil, D. J., Ellett, W., Goodman, S. J., Harrison, S.,
1059 Hawkins, D. L., Heumesser, M., Lin, H., Maskey, M., Schultz, C. J., Stewart, M., ...
1060 Christian, H. (2020). Three years of the lightning imaging sensor onboard the
1061 international space station: Expanded global coverage and enhanced applications.
1062 *Journal of Geophysical Research: Atmospheres*, 125(16).
<https://doi.org/10.1029/2020jd032918>

1063 Boccippio, D. J., Cummins, K. L., Christian, H. J., & Goodman, S. J. (2001). Combined
1064 satellite- and surface-based estimation of the intracloud-cloud-to-ground lightning ratio
1065 over the continental United States. *Monthly Weather Review*, 129(1), 108–122.
[https://doi.org/10.1175/1520-0493\(2001\)129<0108:csasbe>2.0.co;2](https://doi.org/10.1175/1520-0493(2001)129<0108:csasbe>2.0.co;2)

1066 Boggs, L. D., Liu, N., Nag, A., Walker, T. D., Christian, H. J., da Silva, Caitano, L., Austin, M.,
1067 Aguirre, F., & Rassoul, H. K. (2021). Vertical temperature profile of natural lightning
1068 return strokes derived from optical spectra. *Journal of Geophysical Research:
1069 Atmospheres*, 126(8). <https://doi.org/10.1029/2020jd034438>

1070 Brown, S., Janssen, M., Adumitroaie, V., Atreya, S., Bolton, S., Gulkis, S., Ingersoll, A., Levin,
1071 S., Li, C., Li, L., Lunine, J., Misra, S., Orton, G., Steffes, P., Tabataba-Vakili, F.,
1072



1077 Kolmašová, I., Imai, M., Santolík, O., Kurth, W., ... Connerney, J. (2018). Prevalent
1078 lightning sferics at 600 megahertz near Jupiter's poles. *Nature*, 558(7708), 87–90.
1079 <https://doi.org/10.1038/s41586-018-0156-5>

1080 Cardesín Moinelo, A., Abildgaard, S., García Muñoz, A., Piccioni, G., & Grassi, D. (2016). No
1081 statistical evidence of lightning in Venus night-side atmosphere from VIRTIS-Venus
1082 Express Visible observations. *Icarus*, 277, 395–400.
1083 <https://doi.org/10.1016/j.icarus.2016.05.027>

1084 Carvalho, F. L., Uman, M. A., Jordan, D. M., Wilkes, R. A., & Kotovsky, D. A. (2018).
1085 Triggered lightning return stroke luminosity up to 1 km in two optical bands. *Journal of
1086 Geophysical Research: Atmospheres*, 123(17), 9724–9740.
1087 <https://doi.org/10.1029/2018jd028644>

1088 Cecil, D. J., Buechler, D. E., & Blakeslee, R. J. (2014). Gridded lightning climatology from
1089 TRMM-LIS and OTD: Dataset description. *Atmospheric Research*, 135–136, 404–414.
1090 <https://doi.org/10.1016/j.atmosres.2012.06.028>

1091 Christian, H. J., Blakeslee, R. J., Boccippio, D. J., Boeck, W. L., Buechler, D. E., Driscoll, K.
1092 T., Goodman, S. J., Hall, J. M., Koshak, W. J., Mach, D. M., & Stewart, M. F. (2003).
1093 Global frequency and distribution of lightning as observed from space by the Optical
1094 Transient Detector. *Journal of Geophysical Research: Atmospheres*, 108(D1).
1095 <https://doi.org/10.1029/2002jd002347>

1096 Christian, H. J., & Goodman, S. J. (1987). Optical observations of lightning from a high-altitude
1097 airplane. *Journal of Atmospheric and Oceanic Technology*, 4(4), 701–711.
1098 [https://doi.org/10.1175/1520-0426\(1987\)004<0701:oooolfa>2.0.co;2](https://doi.org/10.1175/1520-0426(1987)004<0701:oooolfa>2.0.co;2)

1099 Dyudina, U., Delgenio, A., Ingersoll, A., Porco, C., West, R., Vasavada, A., & Barbara, J.
1100 (2004). Lightning on Jupiter observed in the line by the Cassini imaging science
1101 subsystem. *Icarus*, 172(1), 24–36. <https://doi.org/10.1016/j.icarus.2004.07.014>

1102 Filacchione, G., Haffoud, P., Poulet, F., Piccioni, G., Langevin, Y., Tommasi, L., Barbis, A.,
1103 Carter, J., Guerri, I., Dumesnil, C., De Angelis, S., Vincendon, M., Stefani, S., Pilorget,
1104 C., Tosi, F., & Rodriguez, S. (2024). Calibration of MAJIS (Moons And Jupiter Imaging
1105 Spectrometer). II. Spatial calibration. *Review of Scientific Instruments*, 95(4).
1106 <https://doi.org/10.1063/5.0203872>

1107 Fischer, G., Desch, M., Zarka, P., Kaiser, M., Gurnett, D., Kurth, W., MacHer, W., Rucker, H.,
1108 Lecacheux, A., & Farrell, W. (2006). Saturn lightning recorded by Cassini/RPWS in
1109 2004. *Icarus*, 183(1), 135–152. <https://doi.org/10.1016/j.icarus.2006.02.010>

1110 Fletcher, L.N., Zhang, Z., Brown, S., Oyafuso, F.A., Rogers, J.H., Wong, M.H., Mura, A.,
1111 Eichstadt, G., Orton, G.S., Brueshaber, S., Sankar, R., Li, C., Levin, S.M., Biagiotti, F.,
1112 Guillot, T., Ingersoll, A. P., Grassi, D., Hansen, C.J., Bolton, S., Waite, J.H. (2026).
1113 Structure and Energetics of Jupiter's High-Latitude Storms: Folded Filamentary
1114 Regions Revealed by Juno. *Journal of Geophysical Research: Planets*. in press.

1115 Franzblau, E., & Popp, C. J. (1989). Nitrogen oxides produced from lightning. *Journal of
1116 Geophysical Research: Atmospheres*, 94(D8), 11089–11104.
1117 <https://doi.org/10.1029/jd094id08p11089>

1118 Giles, R. S., Greathouse, T. K., Bonfond, B., Gladstone, G. R., Kammer, J. A., Hue, V.,
1119 Grodent, D. C., Gérard, J., Versteeg, M. H., Wong, M. H., Bolton, S. J., Connerney, J.
1120 E. P., & Levin, S. M. (2020). Possible transient luminous events observed in Jupiter's
1121 upper atmosphere. *Journal of Geophysical Research: Planets*, 125(11).
1122 <https://doi.org/10.1029/2020je006659>

1123 Gjesteland, T., Østgaard, N., Bitzer, P., & Christian, H. J. (2017). On the timing between
1124 terrestrial gamma ray flashes, radio atmospherics, and optical lightning emission.
1125 *Journal of Geophysical Research: Space Physics*, 122(7), 7734–7741.
1126 <https://doi.org/10.1002/2017ja024285>

1127 Goodman, S. J., Blakeslee, R. J., Koshak, W. J., Mach, D., Bailey, J., Buechler, D., Carey, L.,
1128 Schultz, C., Bateman, M., McCaul, E., Jr., & Stano, G. (2013). The GOES-R
1129 Geostationary Lightning Mapper (GLM). *Atmospheric Research*, 125–126, 34–49.
1130 <https://doi.org/10.1016/j.atmosres.2013.01.006>

1131 Gordillo-Vázquez, F. J., & Pérez-Invernón, F. J. (2021). A review of the impact of transient



1132 luminous events on the atmospheric chemistry: Past, present, and future. *Atmospheric*
1133 *Research*, 252, 105432. <https://doi.org/10.1016/j.atmosres.2020.105432>

1134 Gosse, L., Favre, A., Bultel, A., Morel, V., Djurović, S., Simić, N., & Gavanski, L. (2025). In-
1135 depth Stark broadening study of neutral oxygen 777 nm triplet. *Spectrochimica Acta*
1136 *Part B: Atomic Spectroscopy*, 230, 107222. <https://doi.org/10.1016/j.sab.2025.107222>

1137 Gurnett, D. A., Kurth, W. S., Cairns, I. H., & Granroth, L. J. (1990). Whistlers in Neptune's
1138 magnetosphere: Evidence of atmospheric lightning. *Journal of Geophysical Research: Space*
1139 *Physics*, 95(A12), 20967–20976. <https://doi.org/10.1029/ja095ia12p20967>

1140 Gurnett, D. A., Shaw, R. R., Anderson, R. R., Kurth, W. S., & Scarf, F. L. (1979). Whistlers
1141 observed by Voyager 1: Detection of lightning on Jupiter. *Geophysical Research Letters*,
1142 6(6), 511–514. <https://doi.org/10.1029/gl006i006p00511>

1143 Gutsol, K., Nunnally, T., Rabinovich, A., Fridman, A., Starikovsky, A., Gutsol, A., & Potter, R.
1144 W. (2010). Mechanisms of non-equilibrium dissociation of hydrogen sulfide in low-
1145 temperature plasma. *2010 Abstracts IEEE International Conference on Plasma*
1146 *Science*, 1–1. <https://doi.org/10.1109/plasma.2010.5534017>

1147 Haffoud, P., Poulet, F., Vincendon, M., Filacchione, G., Barbis, A., Guiot, P., Lecomte, B.,
1148 Langevin, Y., Piccioni, G., Dumesnil, C., Rodriguez, S., Carter, J., Stefanis, S.,
1149 Tommasi, L., Tosi, F., & Pilorget, C. (2024). Calibration of MAJIS (Moons And Jupiter
1150 Imaging Spectrometer). III. Spectral calibration. *Review of Scientific Instruments*, 95(3).
1151 <https://doi.org/10.1063/5.0188944>

1152 Hutchins, M. L., Holzworth, R. H., Rodger, C. J., & Brundell, J. B. (2012). Far-field power of
1153 lightning strokes as measured by the World Wide Lightning Location Network. *Journal*
1154 *of Atmospheric and Oceanic Technology*, 29(8), 1102–1110.
1155 <https://doi.org/10.1175/jtech-d-11-00174.1>

1156 Ievchenko, I. B., Parnikov, S. G., & Alekseev, V. N. (2019). Variations of the Nightglow 557.7 nm
1157 Emission Intensity during Solar Cycle 23. *Geomagnetism and Aeronomy*, 59(6), 738–
1158 742. <https://doi.org/10.1134/s0016793219050050>

1159 Imai, M., Kolmašová, I., Kurth, W. S., Santolík, O., Hospodarsky, G. B., Gurnett, D. A., Brown,
1160 S. T., Bolton, S. J., Connerney, J. E. P., & Levin, S. M. (2019). Evidence for low
1161 density holes in Jupiter's ionosphere. *Nature Communications*, 10(1).
1162 <https://doi.org/10.1038/s41467-019-10708-w>

1163 Jadhav, D. B., Londhe, A. L., & Bose, S. (1996). Observations of NO₂ and O₃ during
1164 thunderstorm activity using visible spectroscopy. *Advances in Atmospheric Sciences*,
1165 13(3), 359–374. <https://doi.org/10.1007/bf02656853>

1166 Joule, J. P. (1872). Spectrum of lightning. *Nature*, 6(139), 161–161.
1167 <https://doi.org/10.1038/006161b0>

1168 ESA SPICE Service, 2019. JUICE Operational SPICE Kernel Dataset.
1169 <https://doi.org/10.5270/esa-ybmj68p>

1170 Kieu, N., Gordillo-Vázquez, F. J., Passas, M., Sánchez, J., & Pérez-Invernón, F. J. (2021).
1171 High-speed spectroscopy of lightning-like discharges: Evidence of molecular optical
1172 emissions. *Journal of Geophysical Research: Atmospheres*, 126(11).
1173 <https://doi.org/10.1029/2021jd035016>

1174 Kieu, N., Gordillo-Vázquez, F. J., Passas, M., Sánchez, J., Pérez-Invernón, F. J., Luque, A.,
1175 Montanyá, J., & Christian, H. (2020). Submicrosecond spectroscopy of lightning-like
1176 discharges: Exploring new time regimes. *Geophysical Research Letters*, 47(15).
1177 <https://doi.org/10.1029/2020gl088755>

1178 Köhn, C., Heumesser, M., Chanrion, O., Reglero, V., Østgaard, N., Christian, H. J., Lang, T.
1179 J., Blakeslee, R. J., & Neubert, T. (2024). Employing optical lightning data to identify
1180 lightning flashes associated to terrestrial gamma-ray flashes. *Bulletin of Atmospheric*
1181 *Science and Technology*, 5(1). <https://doi.org/10.1007/s42865-024-00065-y>

1182 Kolmašová, I., Imai, M., Santolík, O., Kurth, W. S., Hospodarsky, G. B., Gurnett, D. A.,
1183 Connerney, J. E. P., & Bolton, S. J. (2018). Discovery of rapid whistlers close to Jupiter
1184 implying lightning rates similar to those on Earth. *Nature Astronomy*, 2(7), 544–548.
1185 <https://doi.org/10.1038/s41550-018-0442-z>

1186 Kolmašová, I., Santolík, O., Imai, M., Kurth, W. S., Hospodarsky, G. B., Connerney, J. E. P.,



1187 Bolton, S. J., & Lán, R. (2023). Lightning at Jupiter pulsates with a similar rhythm as in-
1188 cloud lightning at Earth. *Nature Communications*, 14(1).
1189 <https://doi.org/10.1038/s41467-023-38351-6>

1190 Kramida, A. (2009, July 21). *Atomic spectra database*. NIST.
1191 <http://www.nist.gov/pml/data/asd.cfm>

1192 Krider, E.P. (1973). Lightning spectroscopy. *Nuclear Instruments and Methods* 110, 411–419.
1193 [https://doi.org/10.1016/0029-554x\(73\)90720-9](https://doi.org/10.1016/0029-554x(73)90720-9)

1194 Krider, E. P. (1965). Time-resolved spectral emissions from individual return strokes in
1195 lightning discharges. *Journal of Geophysical Research*, 70(10), 2459–2460.
1196 <https://doi.org/10.1029/jz070i010p02459>

1197 Langevin, Y., Poulet, F., Piccioni, G., Filacchione, G., Dumesnil, C., Tosi, F., Carter, J., Barbis,
1198 A., Haffoud, P., Tommasi, L., Vincendon, M., De Angelis, S., Guerri, I., Piloret, C.,
1199 Rodriguez, S., Stefani, S., Bolsée, D., Cisneros, M., Van Laeken, L., ... Carapelle, A.
1200 (2024). Calibration of MAJIS (Moons and Jupiter Imaging Spectrometer). IV.
1201 Radiometric calibration (invited). *Review of Scientific Instruments*, 95(11).
1202 <https://doi.org/10.1063/5.0202702>

1203 Langevin, Y., Zambelli, M., & Guiot, P. (2020). On-board de-spiking implemented by MAJIS,
1204 the VIS/NIR imaging spectrometer of JUICE. *Space Telescopes and Instrumentation*
1205 2020: *Optical, Infrared, and Millimeter Wave*, 239. <https://doi.org/10.1111/12.2562464>

1206 Langford, A. O., Portmann, R. W., Daniel, J. S., Miller, H. L., & Solomon, S. (2004).
1207 Spectroscopic measurements of NO₂ in a Colorado thunderstorm: Determination of
1208 the mean production by cloud-to-ground lightning flashes. *Journal of Geophysical*
1209 *Research: Atmospheres*, 109(D11). <https://doi.org/10.1029/2003jd004158>

1210 Larigalde, S., Labaune, G., & Moreau, J. P. (1981). Lightning leader laboratory simulation by
1211 means of rectilinear surface discharges. *Journal of Applied Physics*, 52(12), 7114–
1212 7120. <https://doi.org/10.1063/1.328420>

1213 Li, D., Luque, A., Gordillo-Vázquez, F. J., Liu, F., Lu, G., Neubert, T., Chanrion, O., Zhu, B.,
1214 Østgaard, N., & Reglero, V. (2021). Blue flashes as counterparts to narrow bipolar
1215 events: the optical signal of shallow in-cloud discharges. *Journal of Geophysical*
1216 *Research: Atmospheres*, 126(13). <https://doi.org/10.1029/2021jd035013>

1217 Li, X., Zhang, J., Chen, L., Xue, Q., & Zhu, R. (2016). Measuring method for lightning channel
1218 temperature. *Scientific Reports*, 6(1). <https://doi.org/10.1038/srep33906>

1219 Liu, F., Lu, G., Neubert, T., Lei, J., Chanrion, O., Østgaard, N., Li, D., Luque, A., Gordillo-
1220 Vázquez, F. J., Reglero, V., Lyu, W., & Zhu, B. (2021). Optical emissions associated
1221 with narrow bipolar events from thunderstorm clouds penetrating into the stratosphere.
1222 *Nature Communications*, 12(1). <https://doi.org/10.1038/s41467-021-26914-4>

1223 López, J. A., Pineda, N., Montanyà, J., Velde, O. van der, Fabró, F., & Romero, D. (2017).
1224 Spatio-temporal dimension of lightning flashes based on three-dimensional Lightning
1225 Mapping Array. *Atmospheric Research*, 197, 255–264.
1226 <https://doi.org/10.1016/j.atmosres.2017.06.030>

1227 Lorenz, R. D. (2018). Lightning detection on Venus: A critical review. *Progress in Earth and*
1228 *Planetary Science*, 5(1). <https://doi.org/10.1186/s40645-018-0181-x>

1229 McCarthy, M. I., Rosmus, P., Werner, H.-J., Botschwina, P., & Vaida, V. (1987). Dissociation
1230 of NH₃ to NH₂+H. *The Journal of Chemical Physics*, 86(12), 6693–6700.
1231 <https://doi.org/10.1063/1.452417>

1232 Narita, T., Wanke, E., Sato, M., Sakanoi, T., Kumada, A., Kamogawa, M., Hirohiko, I., Harada,
1233 S., Kameda, T., Tsuchiya, F., & Kaneko, E. (2018). A study of lightning location system
1234 (Blitz) based on VLF sferics. *2018 34th International Conference on Lightning*
1235 *Protection (ICLP)*, 1–7. <https://doi.org/10.1109/iclp.2018.8503311>

1236 Oliva, F., D'Aversa, E., Migliorini, A., Piccioni, G., Poulet, F., Langevin, Y., Filacchione, G.,
1237 Ciarniello, M., Rodriguez, S., Seignovert, B., Mura, A., Fletcher, L.N., Zinzi, A.,
1238 Giardino, M., Lopinto, E., Sindoni, G., Plainaki, C. (2026). JUICE-MAJIS Earth
1239 observations during the 2024 gravity assist: an overview and comparison with PRISMA
1240 data. *Ann. Geophys.*, submitted to this issue.



1241 Orville, R. E. (1966). High-speed, time-resolved spectrum of a lightning stroke. *Science*,
1242 151(3709), 451–452. <https://doi.org/10.1126/science.151.3709.451>

1243 Orville, R. E. (1968). Spectrum of the lightning stepped leader. *Journal of Geophysical
Research*, 73(22), 6999–7008. <https://doi.org/10.1029/jb073i022p06999>

1244 Pérez-Invernón, F. J., Gordillo-Vázquez, F. J., Passas-Varo, M., Neubert, T., Chanrion, O.,
1245 Reglero, V., & Østgaard, N. (2022). Multispectral optical diagnostics of lightning from
1246 space. *Remote Sensing*, 14(9), 2057. <https://doi.org/10.3390/rs14092057>

1247 Petersen, W. A., Christian, H. J., & Rutledge, S. A. (2005). TRMM observations of the global
1248 relationship between ice water content and lightning. *Geophysical Research Letters*,
1249 32(14). <https://doi.org/10.1029/2005gl023236>

1250 Peterson, M. (2023). Making a Superbolt: Reconciling observations of the optically brightest
1251 lightning on Earth from different satellites. *Earth and Space Science*, 10(8).
1252 <https://doi.org/10.1029/2023ea003001>

1253 Peterson, M., & Rudlosky, S. (2019). The time evolution of optical lightning flashes. *Journal of
1254 Geophysical Research: Atmospheres*, 124(1), 333–349.
1255 <https://doi.org/10.1029/2018jd028741>

1256 Poulet, F., Piccioni, G., Langevin, Y., et al. (2026). ESA/JUICE encounters Earth/Moon in
1257 2024: overview of the Moons And Jupiter Imaging Spectrometer (MAJIS) observations.
1258 *Ann. Geophys.*, submitted to this issue.

1259 Poulet, F., Langevin, Y., & Piccioni, G. (2024). Calibration of the Moons And Jupiter Imaging
1260 Spectrometer (MAJIS): Introduction to the special collection and summary of the
1261 performances. *Review of Scientific Instruments*, 95(7).
1262 <https://doi.org/10.1063/5.0209679>

1263 Poulet, F., Piccioni, G., Langevin, Y., Dumesnil, C., Tommasi, L., Carlier, V., Filacchione, G.,
1264 Amoroso, M., Arondel, A., D'Aversa, E., Barbis, A., Bini, A., Bolsée, D., Bousquet, P.,
1265 Caprini, C., Carter, J., Dubois, J.-P., Condamin, M., Couturier, S., ... Snels, M. (2024).
1266 Moons and Jupiter Imaging Spectrometer (MAJIS) on Jupiter Icy Moons Explorer
1267 (JUICE). *Space Science Reviews*, 220(3). <https://doi.org/10.1007/s11214-024-01057-2>

1268 Prueitt, M. L. (1963). The excitation temperature of lightning. *Journal of Geophysical
1269 Research*, 68(3), 803–811. <https://doi.org/10.1029/jz068i003p00803>

1270 Rafi, M. H., & Mostafa, M. G. (2022). Global lightning phenomena and time series model of
1271 lightning flash radiance. *2022 International Conference on Energy and Power
1272 Engineering (ICEPE)*, 1–6. <https://doi.org/10.1109/icepe56629.2022.10044878>

1273 Rodriguez, S., Vincendon, M., Haffoud, P., Langevin, Y., Poulet, F., Quirico, E., Pilorget, C.,
1274 Filacchione, G., Carter, J., Brunetto, R., Lecomte, B., Guiot, P., Dumesnil, C., &
1275 Piccioni, G. (2024). Calibration of MAJIS (Moons and Jupiter Imaging Spectrometer):
1276 V. Validation with mineral samples and reference materials. *Review of Scientific
1277 Instruments*, 95(10). <https://doi.org/10.1063/5.0215249>

1278 Rudlosky, S. D., Goodman, S. J., Virts, K. S., & Bruning, E. C. (2019). Initial geostationary
1279 lightning mapper observations. *Geophysical Research Letters*, 46(2), 1097–1104.
1280 <https://doi.org/10.1029/2018gl081052>

1281 Ruscic, B. (2015). Active thermochemical tables: Sequential bond dissociation enthalpies of
1282 methane, ethane, and methanol and the related thermochemistry. *The Journal of
1283 Physical Chemistry A*, 119(28), 7810–7837. <https://doi.org/10.1021/acs.jpca.5b01346>

1284 Russell, C. T. (1993). Planetary lightning. *Annual Review of Earth and Planetary Sciences*,
1285 21(1), 43–87. <https://doi.org/10.1146/annurev.ea.21.1050193.000355>

1286 Salanave, L. E. (1964). The optical spectrum of lightning. In *Advances in Geophysics* (pp. 83–
1287 98). Elsevier. [https://doi.org/10.1016/s0065-2687\(08\)60006-0](https://doi.org/10.1016/s0065-2687(08)60006-0)

1288 Salanave, L. E., Orville, R. E., & Richards, C. N. (1962). Slitless spectra of lightning in the
1289 region from 3850 to 6900 Angstroms. *Journal of Geophysical Research*, 67(5), 1877–
1290 1884. <https://doi.org/10.1029/jz067i005p01877>

1291 Schumann, U., & Huntrieser, H. (2007). The global lightning-induced nitrogen oxides source.
1292 *Atmospheric Chemistry and Physics*, 7(14), 3823–3907. [https://doi.org/10.5194/acp-7-3823-2007](https://doi.org/10.5194/acp-7-
1293 3823-2007)

1294 Simpson, J., Kummerow, C., Tao, W.-K., & Adler, R. F. (1996). On the Tropical Rainfall
1295



1296 Measuring Mission (TRMM). *Meteorology and Atmospheric Physics*, 60(1–3), 19–36.
1297 <https://doi.org/10.1007/bf01029783>

1298 Stefani, S., Piccioni, G., Poulet, F., Filacchione, G., Vincendon, M., Barbis, A., Tommasi, L.,
1299 Guerri, I., Langevin, Y., Dumesnil, C., Haffoud, P., Rodriguez, S., Carter, J., Biondi, D.,
1300 Boccaccini, A., De Angelis, S., Tosi, F., Pilorget, C., Guiot, P., & Lecomte, B. (2025).
1301 Calibration of MAJIS (Moons and Jupiter Imaging Spectrometer): VI. The inflight
1302 calibration unit (ICU) (invited). *Review of Scientific Instruments*, 96(1).
1303 <https://doi.org/10.1063/5.0221810>

1304 Uman, M. A., & Orville, R. E. (1964). Electron density measurement in lightning from stark-
1305 broadening of H_α. *Journal of Geophysical Research*, 69(24), 5151–5154.
1306 <https://doi.org/10.1029/jz069i024p05151>

1307 Vincendon, M., Guiot, P., Lecomte, B., Condamin, M., Poulet, F., Arondel, A., Barbay, J.,
1308 Carter, J., De Angelis, S., Dumesnil, C., Filacchione, G., Haffoud, P., Hansotte, J.,
1309 Langevin, Y., Mayeur, P.-L., Piccioni, G., Pilorget, C., Quirico, E., & Rodriguez, S.
1310 (2024). Calibration of MAJIS (Moons And Jupiter Imaging Spectrometer). I. On-ground
1311 setup description and characterization. *Review of Scientific Instruments*, 95(12).
1312 <https://doi.org/10.1063/5.0226567>

1313 Walker, T. D., & Christian, H. J. (2019). Triggered lightning spectroscopy: 2. A quantitative
1314 analysis. *Journal of Geophysical Research: Atmospheres*, 124(7), 3930–3942.
1315 <https://doi.org/10.1029/2018jd029901>

1316 Warwick, J. W., Evans, D. R., Romig, J. H., Alexander, J. K., Desch, M. D., Kaiser, M. L.,
1317 Aubier, M., Leblanc, Y., Lecacheux, A., & Pedersen, B. M. (1982). Planetary radio
1318 astronomy observations from Voyager 2 near Saturn. *Science*, 215(4532), 582–587.
1319 <https://doi.org/10.1126/science.215.4532.582>

1320 Xu, L., Gou, X., Yuan, P., An, T., Jiang, R., & Deng, H. (2024). Spectral study of rare upward
1321 developing, circling, and branching cloud-to-ground lightning. *Journal of Geophysical
1322 Research: Atmospheres*, 129(10). <https://doi.org/10.1029/2023jd040696>

1323 Zarka, P., & Pedersen, B. M. (1986). Radio detection of uranian lightning by Voyager 2.
1324 *Nature*, 323(6089), 605–608. <https://doi.org/10.1038/323605a0>

1325 Zhu, Y., Rakov, V. A., Tran, M. D., Stock, M. G., Heckman, S., Liu, C., Sloop, C. D., Jordan,
1326 D. M., Uman, M. A., Caicedo, J. A., Kotovsky, D. A., Wilkes, R. A., Carvalho, F. L.,
1327 Ngin, T., Gamarota, W. R., Pilkey, J. T., & Hare, B. M. (2017). Evaluation of ENTLN
1328 performance characteristics based on the ground truth natural and rocket-triggered
1329 lightning data acquired in Florida. *Journal of Geophysical Research: Atmospheres*,
1330 122(18), 9858–9866. <https://doi.org/10.1002/2017jd027270>